

# Predictions from Star Formation in the Multiverse

---

**Raphael Bousso and Stefan Leichenauer**

*Center for Theoretical Physics, Department of Physics  
University of California, Berkeley, CA 94720-7300, U.S.A.*

and

*Lawrence Berkeley National Laboratory, Berkeley, CA 94720-8162, U.S.A.*

**ABSTRACT:** We compute trivariate probability distributions in the landscape, scanning simultaneously over the cosmological constant, the primordial density contrast, and spatial curvature. We consider two different measures for regulating the divergences of eternal inflation, and three different models for observers. In one model, observers are assumed to arise in proportion to the entropy produced by stars; in the others, they arise at a fixed time (5 or 10 billion years) after star formation. The star formation rate, which underlies all our observer models, depends sensitively on the three scanning parameters. We employ a recently developed model of star formation in the multiverse, a considerable refinement over previous treatments of the astrophysical and cosmological properties of different pocket universes. For each combination of observer model and measure, we display all single and bivariate probability distributions, both with the remaining parameter(s) held fixed, and marginalized. Our results depend only weakly on the observer model but more strongly on the measure. Using the causal diamond measure, the observed parameter values (or bounds) lie within the central  $2\sigma$  of nearly all probability distributions we compute, and always within  $3\sigma$ . This success is encouraging and rather nontrivial, considering the large size and dimension of the parameter space. The causal patch measure gives similar results as long as curvature is negligible. If curvature dominates, the causal patch leads to a novel runaway: it prefers a negative value of the cosmological constant, with the smallest magnitude available in the landscape.

---

## Contents

<b>1. Introduction</b>	<b>2</b>
<b>2. Making predictions in the landscape</b>	<b>8</b>
2.1 Two choices of measure	8
2.1.1 Causal patch cut-off	9
2.1.2 Causal diamond cut-off	10
2.2 Prior distribution and cosmological selection	11
2.3 Three ways of modeling observers	12
2.3.1 Observers = stars + time delay of 5 or 10 Gyr	13
2.3.2 Observers = entropy production	13
2.4 Summary	14
<b>3. Star formation and entropy production in the multiverse</b>	<b>15</b>
3.1 Star formation	15
3.2 Entropy production	17
<b>4. Results</b>	<b>20</b>
4.1 Weighting by entropy production in the causal diamond	24
4.2 Weighting by star formation + 5 Gyr in the causal diamond	28
4.3 Weighting by star formation + 10 Gyr in the causal diamond	32
4.4 Weighting by entropy production in the causal patch	36
4.5 Weighting by star formation + 5 Gyr in the causal patch	40
4.6 Weighting by star formation + 10 Gyr in the causal patch	44
<b>5. Discussion</b>	<b>48</b>
5.1 Varying the cosmological constant only	48
5.2 Varying spatial curvature only	52
5.3 Varying both the cosmological constant and curvature	55
5.4 Varying the density contrast only	59
5.5 Varying the density contrast and the cosmological constant	61
5.6 Varying the density contrast and spatial curvature	62
5.7 Marginalizing	63

## 1. Introduction

String theory appears to give rise to a large vacuum landscape, containing perhaps ten to the hundreds of metastable vacua with three large spatial dimensions [1, 2]. (See, e.g., Ref. [3] for a discussion of earlier work.) Parameters that appear fundamental at low energies can vary among these vacua and must be predicted statistically. The probability for a particular value is proportional to the expected number of times it is observed. In particular, the cosmological constant,  $\Lambda$ , will vary. Thus, the landscape of string theory provides a theoretical foundation for Weinberg’s [4] famous (and correct) prediction of a small but nonzero value of  $\Lambda$  [1, 5, 6]. In the string landscape, however, not only  $\Lambda$  but also many other parameters are expected to scan. This means that there are many additional opportunities to falsify the theory.

It is legitimate to consider only a subset of the landscape, defined by one variable parameter (such as  $\Lambda$ ), with all other parameters fixed to their observed values. If our observations are highly atypical among the set of observations made in this restricted class of vacua, then the theory is ruled out. If they are typical, then the theory has passed a first test. We can then move on to test the theory further, by predicting a second parameter—for example, the primordial density contrast,  $Q$ . If this succeeds, we have yet another chance to falsify the theory by computing a joint probability distribution over both parameters: now we might find that our universe is very unlikely compared to one in which both parameters differ. If the theory is still not ruled out, we can consider a third parameter (in the present paper, the amount of spatial curvature), and compute yet more probability distributions. Each new probability distribution we compute is another chance for the theory to fail.

In this paper, we present the first detailed computation of a trivariate probability distribution in the landscape. We display all single-variable and bivariate distributions that can be extracted from it.

The computation of such probability distributions is complicated by a number of challenges. What are observers? Given a model for observers, can we actually compute how many observations will be made as a function of the scanning parameters? In this paper, we consider three models for observers, all of which require computing the rate at which stars form, as a function of time. We have recently developed a numerical tool for computing the star formation rate in vacua with different values of  $\Lambda$ ,  $Q$ , and spatial curvature [7]. Here, we apply our star formation model to the challenge of estimating the rate of observations made in this three-parameter space of vacua. As far as we know, this is the first time that the cosmological and astrophysical evolution of other vacua has been modeled at such level of detail.

Another challenge is the measure problem. Long-lived vacua with positive cosmo-

logical constant, which are abundant in the string landscape, lead to eternal inflation [1]. Globally, spatially infinite bubbles of each type of vacuum are produced over and over. Everything that can happen will happen infinitely many times. To compute relative probabilities, such as the ratio of the numbers of times two different parameter values are observed, this divergence has to be regulated.

Recent years have seen considerable progress on the measure problem. Several proposals have been ruled out because they conflict violently with observation [8–18]. Interestingly, several measures that manage to evade the most drastic problems appear to be closely related. They differ at most by subexponential geometric factors [19]. Indeed, some of them have been shown to be precisely equivalent [20,21], despite having superficially a very different form. This apparent convergence is encouraging. It is all the more important to thoroughly test extant proposals, and to discriminate between them, by computing probability distributions and comparing them to observation.

Here, we consider two closely related but inequivalent members of the surviving group of measures: the causal diamond cut-off [22, 23] and the causal patch cut-off [22]. A particularly interesting discovery has been that these two measures provide a novel catastrophic boundary on parameter space, beyond which observations are suppressed—not for dynamical reasons, like galaxy formation, but geometrically. For example, for some values of a scanning parameter, the cut-off region may have exponentially small comoving volume, and for this reason alone will contain a very small number of observers. This geometric effect provides a stronger upper bound on  $\Lambda$  than the disruption of structure [23]. (This result is reproduced here as a special case.) It also provides a stronger constraint on the ratio of dark matter to baryonic matter [24]. In both cases, geometric suppression has significantly improved agreement between theory and observation. The results presented here will reflect the effects of geometric suppression in a larger parameter space, and we will highlight these effects in the discussion of our results (Sec. 5).

**Scope and method** We consider three cosmological parameters: the cosmological constant,  $\Lambda$ ; the primordial density contrast,  $Q \equiv \frac{\delta\rho}{\rho}$ ; and the spatial curvature. We parametrize spatial curvature by the logarithmic quantity  $\Delta N$ , which can be thought of as the number of inflationary  $e$ -foldings minus the minimum number required to explain the observed flatness of our universe. We scan over the three-dimensional parameter space

$$10^{-3}\Lambda_0 < |\Lambda| < 10^5\Lambda_0 \tag{1.1}$$

$$10^{-1}Q_0 < Q < 10^2Q_0 \tag{1.2}$$

$$-3.5 < \Delta N < \infty, \tag{1.3}$$

where  $\Lambda_0$  and  $Q_0$  are the observed values. For each combination  $(\Lambda, Q, \Delta N)$ , we compute a history of structure formation and of star formation in the corresponding universe. We use our own model of star formation [7], which was designed to handle variations of these parameters over several decades. The upper limit on  $Q$  is motivated by a change of regime found in Ref. [7]: For  $Q < 10^2 Q_0$ , most of the star formation happens well after recombination, where we can trust our model; for larger values, we cannot not.

We obtain single- and multivariate probability distributions by computing the expected number of times each parameter combination  $(\Lambda, Q, \Delta N)$  is observed in the multiverse. We consider three different models for observers. One model assumes that the rate of observation tracks the rate of entropy production by stars [22, 23]. The other two are based on the assumption that the rate of observations follows the rate at which stars are produced, with a delay of five or ten billion years.

Our computation is numerical. Even an elementary treatment of the physics of structure formation and star formation involves a complex interplay of different phenomena. In our own universe, several of these processes, such as structure formation, radiative galaxy cooling, Compton cooling of galaxies, galaxy mergers, observer evolution, and vacuum domination, happen roughly on the same time scale, a billion years to within about one order of magnitude. (The lack of any known symmetry that could explain this multiple coincidence is itself evidence for a multiverse [25].) The parameter range we consider includes values in which curvature, too, comes to dominate at a time comparable to the previously mentioned scales. Coincidences of scales preclude a separation into well-defined analytic regimes, necessitating a numerical computation.

Coincidences of scales arise not just for our own universe, but persist on certain hypersurfaces of the parameter space we consider. The time of structure formation scales as  $Q^{-3/2}$ ; the radiative cooling time as  $Q^{-3}$ ; the time of vacuum domination as  $\Lambda^{-1/2}$ ; and the time of curvature domination as  $\exp(3\Delta N)$ . So, for example, in universes whose parameters lie near a certain hypersurface of constant  $Q^3/\Lambda$ , the beginning of structure formation and its disruption by vacuum domination will not be well separated. In the neighborhood of such surfaces, analytical arguments are very imprecise, and numerical treatment is essential.

Numerical computation is somewhat complementary to analytical arguments. Our code becomes unstable when certain separations of scales become too large. This limits the parameter range we can consider numerically. Strictly speaking, our results pertain only to the subset of the landscape defined by the above range of parameters. But for the same reason—a good separation of scales—we can often extrapolate analytically to a larger range. Near some boundaries of our parameter range, the probability density is negligible, and analytic arguments tell us that it will continue to decrease. In these

cases, we can safely neglect the missing part of the probability distribution. We can also do so if the probability density is increasing towards the boundary, but there is a catastrophic change of regime at the boundary that sharply suppresses the number of observations in universes beyond the boundary. (For example, if we increase  $Q$  and  $\Lambda$  while holding  $Q^3/\Lambda$  fixed, eventually vacuum domination will occur before recombination. Since star formation can begin only after recombination, when dark matter halos are exponentially dilute, such universes have negligible probability of being observed.) However, near some boundaries, the probability distribution is increasing and there is no change of regime at or near the boundary. In this case, the probability distribution may be dominated by regions outside the parameter range we consider numerically. In general, we can use analytic arguments to understand its behavior in this regime. An example is the runaway towards small values of  $|\Lambda|$  that we find with the causal patch measure.

**Results** Our results are fully displayed in Sec. 4. Its six subsections correspond to the six combinations of measure and observer model we consider. For each model, we show about 30 plots corresponding to different combinations of parameters that are varied, held fixed, or integrated out. We discuss our results in Sec. 5, where we highlight several interesting features. We provide a qualitative understanding of these features, and we explain how probability distributions depend on the measure and the observer model. Most of our results do not depend strongly on how observers are modeled.<sup>1</sup> However, they do depend on the measure, allowing us to discriminate between the causal diamond and the causal patch. Let us briefly describe our most important findings.

We find that the *causal diamond* measure is in good agreement with observation for all parameter combinations, independently of details of the landscape (see Figs. 2–10). The observed values are within<sup>2</sup>  $2\sigma$  in all plots, except if  $\Lambda$  is scanned over both positive and negative values, and  $Q$  is simultaneously scanned; in this case, they lie within  $2\sigma$  or  $3\sigma$ . This is in large part because the negative range,  $\Lambda < 0$ , is between 12 and 25 times more probable than the positive range, depending on the observer model.

The *causal patch* measure, on the other hand, yields a nonintegrable probability distribution near  $|\Lambda| = 0$  in the absence of a cut-off, i.e., of a smallest possible value of  $|\Lambda|$ . This runaway is explained analytically in Sec. 5.3.<sup>3</sup> The onset of this limiting

---

<sup>1</sup>The case where both  $Q$  and  $\Lambda$  vary is an exception. When observers are modeled by a time delay, larger  $Q$  does not lead to a preference for larger  $\Lambda$ ; with entropy production, it does. In neither case, however, do we find that our values of  $Q$  and  $\Lambda$  are very unlikely.

<sup>2</sup>In some plots they appear just outside of  $2\sigma$ , but by a margin that is negligible compared to the uncertainties in our computation both of probabilities and of the confidence contours.

<sup>3</sup>This result, as well as the preference for large curvature mentioned below, was anticipated in unpublished analytical arguments by Ben Freivogel.

behavior is at  $|\Lambda| \sim t_c^{-2}$ , where  $t_c$  is the time at which curvature comes to dominate. In particular, the runaway does not occur at all in the absence of spatial curvature ( $t_c \rightarrow \infty$ ).

The strength of the runaway depends on the sign of the cosmological constant. For  $\Lambda < 0$ , the probability density grows like  $|\Lambda|^{-1}$  as  $|\Lambda| \rightarrow 0$ , i.e., it grows exponentially in the display variable  $\log_{10}(|\Lambda|/\Lambda_0)$ . The rapid growth is evident in several plots in Figs. 12, 15, and 18. For  $\Lambda > 0$ , the probability density is independent of  $\log_{10}(|\Lambda|/\Lambda_0)$  for  $\Lambda \ll t_c^{-2}$ . Because of our limited parameter range, this milder runaway is not readily apparent in the relevant plots in Figs. 11, 14, and 17, but it can be predicted analytically.

Thus, if spatial curvature is large enough to dominate before  $\Lambda$  does, the causal patch predicts a negative cosmological constant whose magnitude is the *smallest* among all anthropic vacua in the landscape. Whether this runaway is a problem or a success depends on the (unknown) size of the string landscape. It would certainly be a problem if the landscape is so large that it contains anthropic vacua with cosmological constant much smaller than  $\Lambda_0 \sim 10^{-123}$  in magnitude. In this case the causal patch measure would predict at high confidence level that we should find ourselves in a vacuum with  $-\Lambda_0 \ll \Lambda < 0$ , and so would be ruled out. It might be a success, on the other hand, if the observed  $\Lambda$  corresponds to one of the smallest values available among the finite number of anthropic vacua in the landscape. The size of the landscape would be directly responsible for the observed scale  $10^{-123}$ , with the density of its discretuum providing an “ur-hierarchy” from which other hierarchies can be derived [22,25]. Even in this case the causal patch prefers negative values of the cosmological constant (and somewhat larger curvature than the observed upper bound), but only by a factor of order 10, not strongly enough to be ruled out by observation.

At fixed values of  $\Lambda$ , the causal patch leads to a stronger preference for curvature than the causal diamond. This is explained analytically in Sec. 5.3. The pressure is particularly strong for  $\Lambda < 0$ , where the probability density grows very rapidly, like  $\exp(-9\Delta N)$ , towards small values of  $\Delta N$ . This is not a true runaway problem, because there is a catastrophic boundary from the disruption of structure formation that will suppress the probability for sufficiently small values of  $\Delta N$ . However, after  $\Delta N$  is marginalized, this effect would contribute additional weight to vacua with negative cosmological constant even if the runaway towards  $\Lambda = 0$  was suppressed by a lower bound  $\Lambda_{\min} \sim \Lambda_0$  on the magnitude of the cosmological constant from the discretuum.

Thus, we find evidence that the causal patch does not yield probability distributions compatible with observation, unless (1) we are very close to the smallest value of  $|\Lambda|$  in the discretuum ( $\Lambda_{\min} \sim \Lambda_0$ ), or (2) the prior probability distribution differs from what we have assumed (for example, by suppressing curvature so strongly that all

anthropic vacua can be treated as spatially flat,  $t_c \gtrsim \Lambda_{\min}^{-1/2}$ ; this would be the case if all inflationary models in the landscape have a very large number of e-foldings).

Another possibility is worth mentioning. The causal patch measure (with particularly simple initial conditions) was recently shown to be equivalent [21] to the light-cone time cut-off [19] on the multiverse. The latter is motivated [26] by analogy with the holographic UV-IR connection of the AdS/CFT correspondence. The boundary structure in the future of eternally inflating regions differs sharply from that in the future of regions with  $\Lambda \leq 0$ . Since the analogy with AdS/CFT is most compelling in regions with positive cosmological constant, it is natural to consider the possibility that the causal patch measure may give correct relative probabilities only for observations in such regions. This restriction would eliminate the worst of the above problems, which pertain mainly to negative values of  $\Lambda$ . (It would also eliminate the divergence for  $\Lambda = 0$  [27, 28].) There remains a weak (logarithmic) runaway towards  $\Lambda = 0$  from above ( $\Lambda > 0$ ), but this would not be a problem if  $-\log \Lambda_{\min} \sim O(100)$ , a plausible value for the string landscape [1, 29].

**Relation to recent work** Our work can be regarded as a substantial extension and refinement of Ref. [23], where the probability distribution over positive values of  $\Lambda$  was estimated from entropy production in the causal diamond (the “causal entropic principle”). Here we consider a larger number and range of parameters, two different measures, and three different models for observers. Whereas in Ref. [23] the effects of the single parameter  $\Lambda$  on the star formation history were negligible in the most important range of the probability distribution, here we are forced to compute the entire star formation history numerically for each value of  $(\Lambda, Q, \Delta N)$ .

Other interesting extensions of Ref. [23] include Refs. [30–32]. Cline *et al.* [30] compute a bivariate probability distribution over (positive)  $\Lambda$  and  $Q$ ; and Bozek *et al.* [31] compute a bivariate distribution over (positive)  $\Lambda$  and spatial curvature. In principle, these portions of Refs. [30, 31] could be regarded as special cases of the present work, with  $\Lambda > 0$  and either  $\Delta N$  or  $Q$  held fixed, infinities regulated by the causal diamond measure, and observers modeled in terms of the entropy produced by dust heated by stars. However, our results differ because we model star formation and dust temperature differently.

Both [30] and [31] employ the analytic star formation model of Hernquist and Springel (HS) [33]. This model was designed to closely fit data and numerical simulations of the first 13.7 Gyr of our own universe. The HS model exhibits some unphysical features when extrapolated to later times or different values of  $(\Lambda, Q, \Delta N)$ . For example, because it does not take into account the finiteness of the baryon supply in a halo, the HS model predicts unlimited star formation at a constant rate after structure

formation is disrupted by a positive cosmological constant or by negative spatial curvature. Our own star formation model [7] includes only the most important physical effects governing star formation, and so provides only a rough (though surprisingly good) fit of the observed star formation history. However, our model includes not just those effects which govern star formation during the first 13.7 Gyr of our own universe, but is designed to apply in a wide range of  $(\Lambda, Q, \Delta N)$ , and at all times after recombination. Differences between our results and those of Refs. [30,31] can be traced mainly to how we model star formation. A more subtle difference from Ref. [30] arises from our treatment of the dust temperature dependence on the virial density. A trivial difference from Ref. [31] is the choice of prior probability distribution for the parameter  $\Delta N$ . More detail is given in Sec. 2.2.

Salem [34] computes a probability distribution over positive and negative values of  $\Lambda$ , with all other parameters fixed, using the causal patch measure. Observers are modeled as arising at a fixed time delay after the formation of *galaxies* that are similar to the Milky Way in a specific sense [34]. The special case in this paper most similar to Ref. [34] is our computation of a probability distribution over positive and negative  $\Lambda$  with  $Q$  and  $\Delta N$  fixed, using the causal patch measure and modeling observers by a 10 Gyr time delay after star formation. Despite the different observer model, our results for this case agree very well with Salem’s. We find that the observed value of  $\Lambda$  is nearly three standard deviations above the mean of the predicted distribution: 99.7% of observers see a smaller value than ours, and most of them see a negative value. In fact, our observed value of  $\Lambda$  is outside  $2\sigma$  no matter how we model observers, as long as the causal patch is used. (The causal diamond is in better agreement with observation.)

## 2. Making predictions in the landscape

In this section, we will explain how we compute probabilities in the multiverse. We will explore two different measures, described in Sec. 2.1. In Sec. 2.2, we will discuss prior probabilities and cosmological selection effects, and in Sec. 2.3 we will describe three ways of modeling observers. In Sec. 2.4, we will explain how these ingredients are combined to obtain a probability distribution over the parameters  $(\Lambda, Q, \Delta N)$ .

### 2.1 Two choices of measure

Before we can compute anything, we need to remove the divergences that arise in an eternally inflating universe. We will consider two slightly different measures:

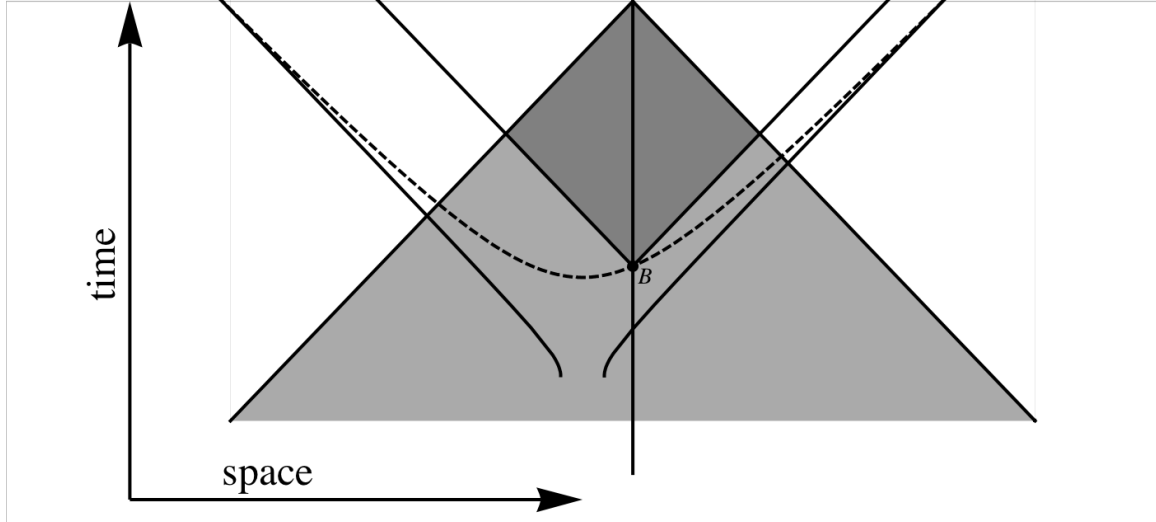


**Figure 1:** The causal patch (shaded triangle) is the past of the future endpoint of a geodesic (vertical line) in the multiverse. The causal diamond (dark shaded) is the intersection of the causal patch with the future of the point  $B$ , where the geodesic intersects a surface of reheating (dashed).

### 2.1.1 Causal patch cut-off

The causal patch is the past of a point on the future boundary of the spacetime (Fig. 1). Consider a pocket universe described by the Friedmann-Robertson-Walker metric

$$ds^2 = -dt^2 + a^2(t) [d\chi^2 + f^2(\chi)d\Omega^2] . \quad (2.1)$$

We consider only open universes (which include flat universes as a special case), so  $f(\chi) = \sinh \chi$ . The causal patch is the set of points with  $\chi < \chi_{\text{patch}}$ , where

$$\chi_{\text{patch}}(t) = \int_t^{t_{\text{max}}} \frac{dt}{a(t)} , \quad (2.2)$$

and  $t_{\text{max}}$  is the time of the crunch. For a long-lived de Sitter vacuum, we can take  $t_{\text{max}} \approx \infty$ .

In any long-lived de Sitter vacuum ( $\Lambda > 0$ ), the patch coincides with the interior of the event horizon, because a late-time decay into a terminal vacuum (with  $\Lambda \leq 0$ ) does not affect the size of the event horizon at early times. In vacua with  $\Lambda < 0$ , the causal patch is the past of a point on the future singularity (the “big crunch”). We will not consider  $\Lambda = 0$  vacua in this paper. The causal patch has divergent four-volume in such vacua [27, 28].

The causal patch cut-off was motivated by the resolution of the quantum xeroxing paradox in black holes [35, 36]. Recently, the measure was shown to be exactly equivalent to the light-cone time cut-off [19, 21], which was motivated by an analogy with the AdS/CFT correspondence [19, 26]. The analogy is most compelling in eternally inflating regions of the multiverse (“eternal domains”). From this viewpoint, it is conceivable that the regime of validity of the causal patch cut-off is limited to vacua with  $\Lambda > 0$ . Our results will offer some phenomenological evidence for this possibility, in that we will find that the measure is least successful in vacua with  $\Lambda < 0$ .

### 2.1.2 Causal diamond cut-off

Consider a geodesic in the multiverse. The causal diamond is the intersection of the causal past of the future endpoint of the geodesic (the causal patch) with the causal future of some earlier point  $B$ . We will follow Ref. [23], where  $B$  was taken to be the point where the geodesic intersects the surface of reheating (Fig. 1). Thus, the causal diamond is the set of points with  $\chi < \chi_{\text{dia}}$ , where

$$\begin{aligned}\chi_{\text{dia}}(t) &= \min\{\chi_{\text{patch}}(t), \eta(t)\} \\ &= \frac{\eta_{\text{max}}}{2} - \left| \frac{\eta_{\text{max}}}{2} - \eta(t) \right| ,\end{aligned}\tag{2.3}$$

where

$$\eta(t) = \int_{t_{\text{rh}}}^t \frac{dt}{a(t)} ,\tag{2.4}$$

and  $\eta_{\text{max}} = \eta(t_{\text{max}})$ .

Because of the additional restriction to the future of  $B$ , the diamond cannot be larger than the patch. With our choice of  $B$ , the diamond will be smaller than the patch approximately until  $\Lambda$ -domination, and it will coincide with the patch after  $\Lambda$ -domination.

Our choice of  $B$  is motivated by the absence of matter prior to reheating. However, the concept of a reheating surface is not completely sharp. Nevertheless, the causal diamond may be an approximation to a more generally defined cut-off; a candidate will be discussed in future work. (In Ref. [22], the point  $B$  was taken to be the starting point of the geodesic on some initial spacelike hypersurface. Then most pocket universes will lie entirely in the future of  $B$ . Except for very unnatural initial conditions, the region excluded from the diamond but present in the patch will be an empty de Sitter region with large cosmological constant. Thus, with this choice, the causal diamond gives the same probabilities as the causal patch.)

## 2.2 Prior distribution and cosmological selection

The probability distribution over an observable parameter  $x$  can be operationally defined as the relative abundance of the various outcomes of all measurements of this parameter in the whole universe.<sup>4</sup> It will be useful for us to think of this probability distribution as a convolution of the following three distributions:

- **Prior distribution.** The relative abundance of different values of the parameter  $x$  among vacua in the theory landscape
- **Cosmological selection effects.** The relative abundance of the different vacua in the universe will differ from the prior distribution because of selection effects of cosmological dynamics and/or initial conditions
- **Anthropic selection effects:** whether, and how frequently, some value of  $x$  is observed may depend on  $x$

Once a measure has been chosen (see the previous subsection), all three distributions listed above can be computed. Let us discuss the first two in turn; we will devote a separate subsection to the third.

**Prior distribution** Because the cosmological constant is effectively a random variable and  $\Lambda = 0$  is not a special point, the prior distribution of  $\Lambda$  can be approximated as flat in the anthropically relevant regime ( $\Lambda \ll 1$ ):

$$\frac{d\tilde{p}}{d\Lambda} \propto 1 \ , \tag{2.5}$$

which translates into a prior proportional to  $\Lambda$  for  $\log_{10} \Lambda$ , our choice of display parameter.

We know much less about the prior distributions of spatial curvature,  $\Delta N$ , and the primordial density contrast,  $Q$ , in the string landscape. There are certain prior distributions which seem implausible, such as a strong preference for large hierarchies (e.g., for small  $\log_{10} Q$  or large  $\Delta N$ ), but this still leaves considerable uncertainty. For definiteness,  $Q$  will be assumed to have a prior which is flat in  $\log_{10} Q$ , which we view as the most optimistic choice among reasonable alternatives:

$$\frac{d\tilde{p}}{d \log_{10} Q} \propto 1 \ . \tag{2.6}$$

For curvature, Ref. [40] estimated

$$\frac{d\tilde{p}}{dN} \propto \frac{1}{N^4} \ . \tag{2.7}$$

---

<sup>4</sup>See, e.g., Refs. [13, 37–39] for discussions of this claim.

We shall use this prior distribution together with the assumption that  $\Delta N = 0$  corresponds to  $N = 60$ .

Despite the large uncertainties about the priors, our results will be robust in the following sense: In cases where we find a tension between the prediction of a measure and observation, this tension could only be removed by choosing a highly implausible prior on  $Q$  or  $\Delta N$ .

**(No) cosmological selection** Relative to the very high energy scales that determine the decay channels and decay rates of metastable landscape vacua, the length of inflation and the mechanism for generating density perturbations can plausibly be assumed to arise at relatively low energies, and thus, to be uncorrelated with the production rate of various vacua. This also holds for the cosmological constant, since we are interested only in an anthropic range of values,  $\Lambda \ll 1$ . These values can only be measured at very low energy density, and so cannot be correlated with the nucleation rate of vacua. Therefore, we will ignore cosmological selection effects.<sup>5</sup>

### 2.3 Three ways of modeling observers

Finally, we must compute the expected number of instances of observing different values of the parameters  $(\Lambda, Q, \Delta N)$  in the cut-off region. In general, these values will be correlated with the presence and number of observers, so we must compute the number of observers as a function of  $(\Lambda, Q, \Delta N)$ . In principle, there is no reason why such a computation could not be performed in a sufficiently powerful theory, by a sufficiently able theorist. In practice, we struggle to define “observer” or “observation” in complete generality. In this paper, we will consider three models for observers. In the first two, we focus on observers “like us”, which arise near a star, a certain number of years (5 Gyr in the first model, 10 Gyr in the second) after the formation of stars. The third model uses entropy production as a more general proxy for observers [22, 23].<sup>6</sup> We will now describe these models in more detail.

---

<sup>5</sup>We assume, however, that there is no “staggering problem” [41, 42], in which cosmological selection effects lead to such unequal probabilities for different vacua as to effectively eliminate most of the landscape and render it unable to solve the cosmological constant problem. The presence of this problem depends on details of the landscape, and in the case of the two local measures considered here, on initial conditions. It is absent in plausible toy models [43, 44].

<sup>6</sup>In combination with the causal diamond cut-off this has been called the “Causal Entropic Principle”. However, we should stress that the question of modeling observers is, at least naively, orthogonal to the measure problem. Entropy production could be used as an observer proxy essentially in any measure.

### 2.3.1 Observers = stars + time delay of 5 or 10 Gyr

We are at liberty to restrict our attention to any class of observers that includes us, for example, observers that emerge near stars. This probably ignores some observers in the landscape. There may be regions without stars that nevertheless contain observers powered by some other source of free energy. However, we can still ask whether our observations are typical of observers in the class we have defined; a theory in which they turn out to be highly atypical can be ruled out.

We need to know both the spatial and temporal location of observations in order to compute what they will observe. Concretely, let us assume that each star, on average, gives rise to some number of observers after a fixed “evolutionary” delay time  $t_{\text{delay}}$ . Then the number of observations made at the time  $t$ , per unit comoving volume and unit time, is

$$\frac{d^2 n_{\text{obs}}}{dV_c dt}(t) \propto \dot{\rho}_*(t - t_{\text{delay}}) , \quad (2.8)$$

where  $\dot{\rho}_*(t) \equiv d^2 m_*/dV_c dt$  is the star formation rate, i.e., the amount of stellar mass produced per unit time and per unit matter mass. Because we assume a fixed initial mass function for stars, this equation holds independently of how the number of observers may depend on the mass of the star, so we will not need to make any particular assumption about this distribution.

In this paper, we explore two choices:  $t_{\text{delay}} = 5 \text{ Gyr}$ , and  $t_{\text{delay}} = 10 \text{ Gyr}$ . The first choice corresponds to the evolutionary timescale of life on earth. It defines a class of observers that are like us in the sense that they exist at equal time delay after the birth of their respective star. In this case, stars with lifetimes less than 5 Gyr do not contribute to observations and should be excluded in Eq. (2.8). However, by the remark at the end of the previous paragraph, this only affects the constant of proportionality in Eq. (2.8), but not the normalized probability distributions.

The second choice defines a slightly different class of observers, which are like us in the sense that they exist 10 Gyr after *most* stars in the universe are produced. (In our universe, the peak of the star formation rate was about 10 Gyr ago.)

### 2.3.2 Observers = entropy production

The second law of thermodynamics guarantees that the spontaneous formation of an ordered subsystem (like a frozen pond, or a galaxy) will be compensated by increased entropy in the remaining system. In practice, this increase tends to overcompensate vastly, and the overall entropy increases. This motivated one of us to propose [22] that the emergence of complex structures such as observers is correlated with the production of entropy. The simplest ansatz is that the rate of observation is proportional (on

average) to the rate of entropy production:

$$\frac{d^2 n_{\text{obs}}}{dV_c dt}(t) \propto \frac{d^2 S}{dV_c dt}(t) . \quad (2.9)$$

In Ref. [23], it was shown that most of the entropy produced inside the causal diamond in our universe comes from dust heated by stars. In the absence of complex molecules, let alone stars and galaxies, the entropy production would be much lower. The simple criterion of entropy production thus turns out to capture several conditions often assumed explicitly to be necessary for life. Moreover, it succeeds very well in postdicting our rather unusual location: If life is correlated with entropy production, then most life forms will find themselves when and where most entropy production takes place: near stars, during the era while stars are burning. Indeed, the probability distribution over positive values of  $\Lambda$  computed from the causal entropic principle (weighting by entropy production in the causal diamond) proved to be in excellent agreement with observation [23].

Here we refine and extend the validity of that prescription. We will use the star formation rates calculated according to Ref. [7] in order to properly account for the changes in star formation as cosmological parameters are varied. In addition, we will account for the dependence of the dust temperature on the virial density.

In contrast to the causal diamond, overall entropy production in the causal patch is dominated by the entropy produced at reheating. This is evidently not a good proxy for observers. In the context of the causal patch cut-off, we will model observers specifically in terms of the entropy produced by dust heated by stars (or, as above, by a time delay).

## 2.4 Summary

The rate of observation, per unit comoving volume and unit time, in a universe with parameters  $(\Lambda, Q, \Delta N)$  is given by

$$\frac{d^2 n_{\text{obs}}}{dV_c dt}(t; \Lambda, Q, \Delta N) \propto \begin{cases} \frac{d^2 S}{dV_c dt}(t; \Lambda, Q, \Delta N) & \text{(entropy production)} \\ \dot{\rho}_*(t - 5 \text{ Gyr}; \Lambda, Q, \Delta N) & \text{(star formation plus 5 Gyr)} \\ \dot{\rho}_*(t - 10 \text{ Gyr}; \Lambda, Q, \Delta N) & \text{(star formation plus 10 Gyr)} \end{cases} \quad (2.10)$$

depending on which model for observers we use; see Sec. 2.3. In the second (third) case, we set the rate of observation to zero for  $t < 5$  Gyr ( $t < 10$  Gyr).

The total number of observations in a universe with parameters  $(\Lambda, Q, \Delta N)$  is given by integrating the above rate over the time and comoving volume contained in

the causal patch or causal diamond:

$$n_{\text{obs}}(\Lambda, Q, \Delta N) = \int_0^\infty dt V_c(t) \frac{d^2 n_{\text{obs}}}{dV_c dt}(t; \Lambda, Q, \Delta N) , \quad (2.11)$$

where the comoving volume at time  $t$  is given by

$$V_c(t) = \begin{cases} \int_0^{\chi_{\text{patch}}(t)} d\chi \, 4\pi \sinh^2 \chi & \text{(causal patch measure)} \\ \int_0^{\chi_{\text{diamond}}(t)} d\chi \, 4\pi \sinh^2 \chi & \text{(causal diamond measure)} \end{cases} \quad (2.12)$$

and  $\chi_{\text{patch}}$  and  $\chi_{\text{diamond}}$  are given in Eqs. (2.2) and (2.3).

The probability distribution over  $(\Lambda, Q, \Delta N)$  is obtained by multiplying the prior probability for a universe with  $(\Lambda, Q, \Delta N)$ , discussed in Sec. 2.2, by the number of observations made in such a universe:

$$\frac{d^3 p}{d \log \Lambda d \log_{10} Q d(\Delta N)} = \frac{\Lambda}{(60 + \Delta N)^4} n_{\text{obs}}(\Lambda, Q, \Delta N) . \quad (2.13)$$

With three choices of observer model and two choices of measure, we thus consider a total of six different models for computing probabilities in the multiverse.

### 3. Star formation and entropy production in the multiverse

In this section we describe in detail how we compute the quantities appearing in Eq. (2.10). In Sec. 3.1 we review our star formation model [7]. In Sec. 3.2, we estimate the rate of entropy production by the dust heated by stars, following [23, 45].

#### 3.1 Star formation

To compute the rate of star formation per unit time and unit comoving volume in a universe with parameters  $(\Lambda, Q, \Delta N)$ ,

$$\dot{\rho}_*(t; \Lambda, Q, \Delta N) \equiv \frac{d^2 m_*}{dV_c dt} , \quad (3.1)$$

we use the model we developed in Ref. [7]. The following summary will skip many details, and the reader is encouraged to consult Ref. [7] for a more thorough discussion. There are three steps to star formation: (1) density perturbations grow and collapse to form dark matter halos; (2) baryons trapped in the halo cool and condense; (3) stars form from the cooled gas.

Cosmological perturbations can be specified by a time-dependent power spectrum,  $\mathcal{P}$ , which is a function of the wavenumber of the perturbation,  $k$ . The r.m.s. fluctuation

amplitude,  $\sigma$ , within a sphere of radius  $R$ , is defined by smoothing the power spectrum with respect to an appropriate window function:

$$\sigma^2 = \frac{1}{2\pi^2} \int_0^\infty \left( \frac{3 \sin(kR) - 3kR \cos(kR)}{(kR)^3} \right)^2 \mathcal{P}(k) k^2 dk . \quad (3.2)$$

The radius  $R$  can be exchanged for the mass  $M$  of the perturbation, using  $M = 4\pi\rho_m R^3/3$ . Generally  $\sigma$  factorizes as

$$\sigma(M, t) = Q s(M) G(t) . \quad (3.3)$$

$Q$  sets the overall scale of density perturbations, and is one of the parameters we vary. The scale dependence  $s(M)$  is held fixed; we use the fitting formula provided in Ref. [46]:

$$s(M) = \left[ (9.1\mu^{-2/3})^{-0.27} + (50.5 \log_{10} (834 + \mu^{-1/3}) - 92)^{-0.27} \right]^{-1/0.27} \quad (3.4)$$

with  $\mu = M/M_{\text{eq}}$ , where

$$M_{\text{eq}} = 1.18 \times 10^{17} m_\odot \quad (3.5)$$

is roughly the mass contained inside the horizon at matter-radiation equality. The linear growth function  $G(t)$  satisfies

$$\frac{d^2 G}{dt^2} + 2H \frac{dG}{dt} = 4\pi G_N \rho_m G \quad (3.6)$$

with the initial conditions  $G = 5/2$  and  $\dot{G} = 3H/2$  at  $t = t_{\text{eq}}$ . For each value of  $\Lambda$  and  $\Delta N$ , we numerically compute the scale factor  $a(t)$  and, from Eq. (3.6),  $G(t)$ .

Density perturbations grow and collapse to form structure. The Press-Schechter function,  $F$ , gives the total fraction of mass collapsed into structures of mass  $< M$  [47]:

$$F(< M, t) = \text{Erf} \left( \frac{1.68}{\sqrt{2}\sigma(M, t)} \right) . \quad (3.7)$$

We can compute the mass density of a collapsed halo (called the virial density,  $\rho_{\text{vir}}$ ) using the spherical top-hat collapse model. The virial density does not depend on the mass of the object, but only on the time of collapse.

After collapse, the baryonic component of a halo must cool and undergo further condensation before stars can form. We require that this cooling process happen sufficiently quickly. The most efficient cooling mechanisms require ionized gas, so only those halos with a virial temperature above  $10^4$  K can cool further. This translates into a time-dependent lower mass limit for star-forming halos. Also, we require that halos cool on a timescale faster than their own gravitational timescale,  $t_{\text{grav}} = (G_N \rho_{\text{vir}})^{-1/2}$ .

This is motivated by observations indicating that cooling-limited galaxy formation is ineffective, providing a time-dependent upper mass limit on star-forming halos.

A halo in the allowed mass range is assigned an individual star formation rate based on its mass and time of virialization:

$$\frac{dm_{\star}^{\text{single}}}{dt}(M, t_{\text{vir}}) = \frac{1}{6} \sqrt{\frac{32}{3\pi}} \frac{M}{t_{\text{grav}}(t_{\text{vir}})} . \quad (3.8)$$

We use the extended Press-Schechter formalism [48] to sum over the formation times of all halos of mass  $M$  in existence at time  $t$ :

$$\frac{dm_{\star}^{\text{avg}}}{dt}(M, t) = \frac{1}{6} \sqrt{\frac{32}{3\pi}} \int_{t_{\text{min}}}^{t_{\text{max}}} \left[ \frac{M}{t_{\text{grav}}(t_{\text{vir}})} \frac{\partial P}{\partial t_{\text{vir}}}(t_{\text{vir}}, M, t) \right] dt_{\text{vir}} . \quad (3.9)$$

The function  $P$  is the probability that a halo of mass  $M$  at time  $t$  virialized before  $t_{\text{vir}}$ , and is derived in Ref. [48]:

$$P(< t_{\text{vir}}, M, t) = \int_{M/2}^M \frac{M}{M_1} \frac{d\beta}{dM_1}(M_1, t_{\text{vir}}, M, t) dM_1 , \quad (3.10)$$

where

$$\beta(M_1, t_1, M_2, t_2) = \text{Erfc} \left( \frac{1.68}{Q \sqrt{2(s(M_1)^2 - s(M_2)^2)}} \left( \frac{1}{G(t_1)} - \frac{1}{G(t_2)} \right) \right) . \quad (3.11)$$

$t_{\text{min}}$  and  $t_{\text{max}}$  are specific functions of  $M$  and  $t$  designed to restrict the range of integration to only those halos which are capable of cooling and have not yet used up all of their cold gas supply [7].

Finally, the star formation rate itself is given by summing over all values of halo mass, weighted by the Press-Schechter distribution function:

$$\dot{\rho}_{\star}(t; \Lambda, Q, \Delta N) = \sqrt{\frac{8}{27\pi}} \int dM \int_{t_{\text{min}}}^{t_{\text{max}}} dt_{\text{vir}} \frac{\partial F}{\partial M}(M, t) \frac{1}{t_{\text{grav}}(t_{\text{vir}})} \frac{\partial P}{\partial t_{\text{vir}}}(t_{\text{vir}}, M, t) . \quad (3.12)$$

### 3.2 Entropy production

As explained in Sec. 2.3, we model the rate of observation either by the rate star formation plus a time delay, or by the rate of entropy production by stars. A time delay is trivial to implement: we simply shift the star formation rate by 5 or 10 Gyr. Here we will discuss how to estimate the rate of entropy production per unit comoving volume and unit time. The entropy production rate at the time  $t$  is given by the total

luminosity of the stars shining at that time, divided by the effective temperature at which this power is ultimately dissipated. A significant fraction of starlight is absorbed by interstellar dust grains and re-emitted in the infrared. This process converts one optical photon into many infrared photons, so it dominates entropy production [23]. Hence, the appropriate temperature is the interstellar dust temperature.

We will follow Ref. [23] for computing the total luminosity at time  $t$  from the star formation rate at earlier times. We will follow Ref. [45] for estimating the temperature of dust at time  $t$  in a galaxy that formed at time  $t_f$ . This doubly time-dependent treatment of the dust temperature is a refinement over Ref. [23], where the temperature was held fixed.

We take the luminosity of an individual star to be related to its mass by  $L_\star \propto m^{3.5}$ . The mass distribution of newly formed stars is assumed to be described by the Salpeter initial mass function, independently of time and of the parameters  $(\Lambda, Q, \Delta N)$ :

$$\xi_{\text{IMF}}(m) \equiv \frac{dN_\star}{dm} = \begin{cases} am^{-2.35} & \text{if } m > 0.5 m_\odot \\ bm^{-1.5} & \text{if } m \leq 0.5 m_\odot \end{cases} \quad (3.13)$$

No stars form ( $\xi_{\text{IMF}}(m) = 0$ ) outside the range  $0.08 m_\odot < m < 100 m_\odot$ . Here  $a$  and  $b$  are constants chosen so that the function is continuous and integrates to one over the allowed mass range.

The lifetime of a star is also controlled by its mass; smaller stars live longer. It is convenient to work with the inverted relation [23]:

$$m_{\text{max}}(\Delta t) = \begin{cases} 100 m_\odot & \text{if } \Delta t < 10^{-4} \text{ Gyr} ; \\ \left(\frac{10 \text{ Gyr}}{\Delta t}\right)^{2/5} m_\odot & \text{if } \Delta t \geq 10^{-4} \text{ Gyr} , \end{cases} \quad (3.14)$$

where  $m_{\text{max}}(\Delta t)$  is the mass of the largest survivors in an ensemble of stars created a time  $\Delta t$  ago. Setting  $m_{\text{max}} = 0.08 m_\odot$  corresponds to  $\Delta t = 8^{-5/2} 10^6 \text{ Gyr} \approx 5500 \text{ Gyr}$ , the lifetime of the longest-lived stars.

Now consider an ensemble of stars of total mass  $dm_\star$  that formed at the time  $t_f$ . Their combined luminosity at the time  $t = t_f + \Delta t$  is independent of  $t_f$  and is given by

$$\frac{dL}{dm_\star}(\Delta t) = \frac{1}{\langle m \rangle} \int_{0.08 m_\odot}^{m_{\text{max}}(\Delta t)} dm \xi_{\text{IMF}}(m) L_\odot \left(\frac{m}{m_\odot}\right)^{3.5} . \quad (3.15)$$

The mass and luminosity of the sun,  $m_\odot$  and  $L_\odot$ , and the average initial mass,  $\langle m \rangle$ , are constant and drop out in all normalized probabilities. We will continue to display them for clarity.

Next, we turn to estimating the temperature of interstellar dust, at which this luminosity is ultimately dissipated. The dust temperature will depend on the mass

density of the host galaxy (higher density means higher temperature), and on the CMB temperature. The CMB temperature is borderline negligible in our universe. But in a large portion of our parameter space (specifically, for  $Q > Q_0$ ), significant star formation occurs earlier than in our universe. Then the CMB temperature can be larger than the temperature the dust would reach just from stellar heating, and so it can effectively control the dust temperature. This is an important effect mitigating the preference for larger values of  $Q$  [45].

Ref. [49] [see Eq. 170 therein] models how the temperature of the interstellar dust scales with the distance to a star:<sup>7</sup>

$$T(t_{\text{vir}}, t)^6 \propto \left( \frac{R_\star}{R(t_{\text{vir}})} \right)^2 T_\star^5 + T_{\text{CMB}}(t)^5, \quad (3.16)$$

where we have included the last term to account for the heating of dust by the CMB. Here,  $R$  is a typical distance between stars, and  $T_\star$  is a typical stellar temperature (we use 6000 K). We are explicitly dropping an overall dimensionful factor because we are only interested in normalized probabilities. One expects the interstellar distance to scale inversely with the density of the host galaxy, which in turn is proportional to the virial density of halo:

$$R^3 \propto \rho_{\text{vir}}^{-1}. \quad (3.17)$$

We normalize to the value  $(R_\star/R)^2 = 3.5 \times 10^{-14}$  for our galaxy [49], which we assume formed with a virial density typical of halos forming at  $t_{\text{vir}} = 3.7$  Gyr. Then Eq. (3.17) determines the relevant  $R$  for other galaxies that form at different times in our universe or in others. Note that the virial density is set by the time  $t_{\text{vir}}$  of the last major merger, whereas the CMB temperature appearing in Eq. (3.16) must be evaluated at the time of emission. In our model, stars do not form for a long time after virialization,

$$\frac{t_f - t_{\text{vir}}}{t_{\text{vir}}} \lesssim 1, \quad (3.18)$$

Thus we can approximate  $t_{\text{vir}} \approx t_f$  for the purposes of estimating the relevant dust temperature, leaving us with one fewer time variable to keep track of.

To compute the entropy production rate, at the time  $t = t_f + \Delta t$ , per unit stellar

---

<sup>7</sup>The powers of temperature in this relation arise because the dust neither absorbs nor emits as a blackbody. However, our results would not change much if we adopted the blackbody ansatz  $T^4 = \left(\frac{R_\star}{R}\right)^2 T_\star^4 + T_{\text{CMB}}^4$ . This is reassuring since the regime of validity of Eq. (3.16) depends on material properties which are difficult to estimate.

mass formed at the time  $t_f$ , we divide the luminosity by the temperature:

$$\frac{d^2 S}{dm_\star dt}(t, t_f) = \frac{1}{T(t_f, t_f + \Delta t)} \frac{dL}{dm_\star}(\Delta t) \quad (3.19)$$

$$= \frac{1}{T(t_f, t)} \frac{L_\odot}{\langle m \rangle} \int_{0.08 m_\odot}^{m_{\max}(t-t_f)} dm \xi_{\text{IMF}}(m) \left( \frac{m}{m_\odot} \right)^{3.5}. \quad (3.20)$$

From this rate we can obtain the total entropy production rate at the time  $t$ , by integrating over  $t_f$  and using the SFR to account for the amount of stellar mass produced per comoving volume at the time  $t_f$ :

$$\frac{d^2 S}{dV_c dt}(t) = \int_0^t dt_f \frac{d^2 S}{dm_\star dt}(t, t_f) \dot{\rho}_\star(t_f). \quad (3.21)$$

By Eq. (2.10), this becomes the integrand in Eq. (2.11) in the case where observers are modeled by entropy production.<sup>8</sup>

## 4. Results

This section contains the probability distributions we have computed over the parameters  $\Lambda, Q, \Delta N$ .

**Ordering** There are six subsections, corresponding to the six models described in Sec. 2 (two different measures, and three different ways of modeling observers). Each subsection contains three pages of plots. On the first page,  $\Lambda$  runs only over positive values; on the second,  $\Lambda < 0$ . This division is useful since some of the interesting

---

<sup>8</sup>Numerically, the resulting double integral is most efficiently evaluated by exchanging the order of integration:

$$n_{\text{obs}} \propto \int_0^\infty dt V_c(t) \frac{d^2 S}{dV_c dt}(t) \quad (3.22)$$

$$= \int_0^\infty dt \int_0^t dt_f V_c(t) \frac{d^2 S}{dm_\star dt}(t, t_f) \dot{\rho}_\star(t_f) \quad (3.23)$$

$$= \int_0^\infty dt_f \int_{t_f}^\infty dt V_c(t) \frac{d^2 S}{dm_\star dt}(t, t_f) \dot{\rho}_\star(t_f) \quad (3.24)$$

$$= \int_0^\infty dt_f \left[ \int_0^\infty d(\Delta t) V_c(t_f + \Delta t) \frac{d^2 S}{dm_\star dt}(t_f + \Delta t, t_f) \right] \dot{\rho}_\star(t_f). \quad (3.25)$$

The inner integral represents the entropy that will eventually be produced inside the causal patch or diamond by the stars created at time  $t_f$ . Because it does not depend on  $Q$ , it is more efficient to compute this integral separately as a function of  $(t_f; \Lambda, \Delta N)$ , before multiplying by  $\dot{\rho}_\star(t_f; \Lambda, Q, \Delta N)$  and computing the outer integral.

features we find depend on the sign of the cosmological constant. Moreover, visually the clearest way to display the probability distribution over  $\Lambda$  is as a function of  $\log_{10} |\Lambda|$ , which makes it difficult to include  $\Lambda = 0$ . On the third page of each subsection, we display some distributions over all values of  $\Lambda$ .

We have computed a full trivariate probability distribution for each case, which cannot be displayed in a single plot. For this reason, the first page ( $\Lambda > 0$ ) and second page ( $\Lambda < 0$ ) of every subsection contain 12 plots each. The first six plots (the top two rows of plots) are single variable distributions over  $\Lambda$ , over  $Q$ , and over  $\Delta N$ . In the first three, the remaining two variables are held fixed. This corresponds to asking about the probability distribution over a single parameter in the portion of the landscape in which the two other parameters take the observed values. In the second group of three plots, the remaining two variables are marginalized (i.e., integrated out). This corresponds to asking about the probability distribution over a single parameter in the entire three-parameter landscape we consider.

The remaining six plots on each page are bivariate probability distributions. Of these, the first three are distributions over two parameters with the third held fixed. This corresponds to asking about a bivariate probability distribution in the portion of the landscape in which the remaining parameter takes its observed value. In the other three bivariate plots, the remaining variable is integrated out. This corresponds to asking about the probability distribution over some pair of parameters in the entire three-parameter landscape we consider.

The third page of each subsection shows distributions in which  $\Lambda$  takes both positive and negative values, either explicitly or by marginalization. The three plots in which  $\Lambda$  is fixed to the observed value would be identical to the corresponding plots shown on the  $\Lambda > 0$  page. Moreover, we do not display any plots corresponding to a parameter combination that led to a pathological probability distribution for either  $\Lambda > 0$  or  $\Lambda < 0$ , when the inclusion of both signs can only worsen the problem. (This case arises for the causal patch only.)

**Confidence regions** In most plots (see the discussion below), we show the one-sigma (68% confidence) and two-sigma (95% confidence) parameter regions. The one-sigma region is unshaded, the two-sigma region is lightly shaded, and the remaining region is shaded dark. In the one-parameter plots, confidence regions are centered on the median of the probability distribution. In the two parameter plots, they are centered on the maximum probability density and bounded by contour lines of constant probability. Additional contours are included for better visualization of the probability distribution. They not drawn at any special values of the probability density or of its integral.

The displayed confidence regions are strictly based on the probability distribution

over the portion of the landscape for which we have computed probabilities:

$$10^{-3}\Lambda_0 < |\Lambda| < 10^5\Lambda_0 \quad (4.1)$$

$$10^{-1}Q_0 < Q < 10^2Q_0 \quad (4.2)$$

$$-3.5 < \Delta N < \infty, \quad (4.3)$$

with all other physical parameters held fixed. In other words, we are setting the probability to zero outside the above range, and for universes in which other parameters differ from ours. As we noted in the introduction, this is legitimate: we are asking whether or not our observations are typical among those made by observers in this portion of the landscape, described by a particular range of three particular parameters. If they are highly atypical, then there is a problem.

In certain plots involving  $\Lambda < 0$  with the causal patch measure, the probability density increases very rapidly towards the boundary of our parameter range. Because of this runaway behavior, the 1 and  $2\sigma$  regions would depend sensitively on the precise value of the parameter boundary. In these cases, we do not display confidence intervals in single-variable plots; in bivariate plots, we display only the contours of constant probability density, along with an arrow indicating the direction of increasing probability density. Other runaways are less strong; in this case we do display confidence intervals based on the above parameter range. Finally, not every probability distribution that increases monotonically towards a boundary is indicative of a runaway, because it might be cut off by a change of regime at finite distance beyond the boundary: For any value of  $Q$  and  $\Lambda$ , sufficiently large curvature will disrupt structure formation. And for any  $\Delta N$  and  $\Lambda$ , sufficiently large  $Q$  (of order the upper bound we consider,  $10^2Q_0$ ) leads to a change of regime. We will note in the captions which plots have a true runaway direction.

**Display range and data point** We display the entire range of parameters for which we have computed the probability density, Eq. (4.3), except, of course, for  $\Delta N$ , where we cut off the display at  $\Delta N = 1$ . For larger values of  $\Delta N$ , curvature is too weak to affect either the dynamics of structure formation or the geometry of the causal patch or diamond. In this regime, the probability distribution over  $\Delta N$  is proportional to the prior distribution, Eq. (2.7). All contour intervals take this undisplayed portion of the probability distribution into account. Also, when we marginalize over  $\Delta N$ , the undisplayed portion is included in the range of the integral.

The display variables are not  $\Lambda$ ,  $Q$ , and  $\Delta N$ , but  $\log_{10}(|\Lambda|/\Lambda_0)$ ,  $\log_{10}(Q/Q_0)$ , and  $\Delta N$ . Therefore, the observed values correspond to 0 on every axis. To guide the eye, the vertical axis intersects the horizontal axis at 0 in all single-parameter plots, so the

observed value is where the vertical axis is. In the two-parameter plots, the data point  $(0, 0)$  is shown by a green triangle.

There are two subtleties: First, in the figures that display only the negative range of  $\Lambda$ , the observed (positive) value cannot be shown. We find it useful to show as “data” our “evil twin” universe, with  $\Lambda = -\Lambda_0$ ,  $Q = Q_0$ , and  $\Delta N \geq 0$ , in these plots. Secondly, spatial curvature has not been detected, only constrained. Thus,  $\Delta N = 0$  corresponds to a lower bound, and not to the actual value of  $\Delta N$  in our universe. The reader should keep in mind, therefore, that in single-variable plots over  $\Delta N$  the entire region to the right of the vertical axis is compatible with observation. In two-parameter plots involving  $\Delta N$ , the observed universe lies somewhere on a semi-infinite line starting at the triangle and running upward towards larger  $\Delta N$ . As long as some part of the  $\Delta N \geq 0$  range is not very improbable, there would be no conflict with experiment, even if the point  $\Delta N = 0$  were highly improbable.

**Comparing the probability distributions to observation** Because life is short, we reject scientific theories with finite confidence only, taking a gamble that freak chance might be leading us astray. Often, we can increase our confidence by repeating experiments. In cosmology, we sometimes cannot. This limitation has nothing to do with the multiverse, but stems from the finiteness of the observable universe. (Because  $\Lambda_0 \neq 0$ , the observable universe will not grow indefinitely, so this is not merely an accident of our present era.) For example, cosmic variance does not prevent us from drawing conclusions from the CMB, but it does prevent us from sharpening them when they do not meet a confidence standard we are comfortable with, as may be the case for the low quadrupole.

There is one data point for each parameter considered in this paper, the value observed in our universe (or, in the case of  $\Delta N$ , the range not ruled out). If this data point happened to have very small probability (e.g., if it lay well beyond  $6\sigma$ , if this were our desired level of confidence), then our observations would be extremely unexpected given the theory from which the probability distribution was computed. In other words, the theory would conflict with experiment at that level of confidence. Since the theory consists of a combination of a prior distribution in the landscape (including the possible range of parameters), a choice of measure, and a choice of observer model, at least one of these elements is excluded.

**Main conclusions** Our conclusions are more fully described in the introduction. The causal diamond measure is remarkably successful. The observed values of parameters lie in the  $2\sigma$  confidence region of all but one or two out of thirty-three probability distributions we show for each observer model (where they lie within  $3\sigma$ ).

The causal patch is problematic, independently of the observer model. In the absence of curvature, results are similar to the causal diamond, if not quite as successful quantitatively. In the presence of curvature, we find significant conflicts between prediction and observation. They are sharpest in distributions that include negative values of  $\Lambda$  (see, e.g., Fig. 16), where we find a strong runaway towards small  $|\Lambda|$  and strong pressure towards the large-curvature boundary on structure formation. If we restrict to positive  $\Lambda$ , there is still a weak runaway to small positive values of  $\Lambda$ , though this is barely visible in the parameter range we display. As discussed in the introduction, these runaways imply that the causal patch measure is incorrect, or that the prior probabilities differ significantly from those we have assumed, or that the finite size of the landscape effectively provides a cut-off on how small  $\Lambda$  can be, and that we find ourselves near this cut-off. The level of confidence at which the measure is excluded by the data depends sensitively on this cut-off; with no cut-off, it is infinite.

#### 4.1 Weighting by entropy production in the causal diamond

With this observer model and measure, the observed parameters fall within the central  $2\sigma$  of almost all probability distributions we compute. The only exceptions are the bivariate distributions over  $Q$  and the full range of  $\Lambda$  (both positive and negative  $\Lambda$ ), where we find ourselves outside of  $2\sigma$  but within  $3\sigma$  (6th and 9th plot, Fig. 4). The total probability for  $\Lambda < 0$  is 25 times larger than that for  $\Lambda > 0$  when  $Q = Q_0$  and  $\Delta N > 0$  are held fixed, and 11 times larger when  $Q$  and  $\Delta N$  are marginalized (1st and 2nd plot, Fig. 4).

As explained in Sec. 5.4, the distribution over  $Q$ , with  $\Lambda = \Lambda_0$  and  $\Delta N > 0$ , has a maximum centered on the observed value (2nd plot, Fig. 2). This feature is not reproduced with any other choice of measure or observer model. However, this does not in itself lend particular weight to this measure and observer model. Any model in which the observed value falls, say, within  $2\sigma$  should be regarded as unproblematic.

As explained in Sec. 5.5, the most likely value of  $Q$  grows with  $\Lambda$  (9th and 12th plot, Fig. 2); therefore, the observed value of  $Q$  is no longer the most likely after  $\Lambda$  is integrated out (5th plot, Fig. 2), though it is well within  $2\sigma$ .

For  $\Lambda = \Lambda_0$ , the 3rd plot in Fig. 2 shows that too much curvature suppresses structure formation: the probability distribution increases towards smaller  $\Delta N$  (governed mainly by the prior distribution), but turns around near  $\Delta N = -2$ . For negative cosmological constant (Fig. 3), the analogous plot does not show this feature because the turnaround occurs just outside our display range. The reason for this difference is discussed in Sec. 5.3.

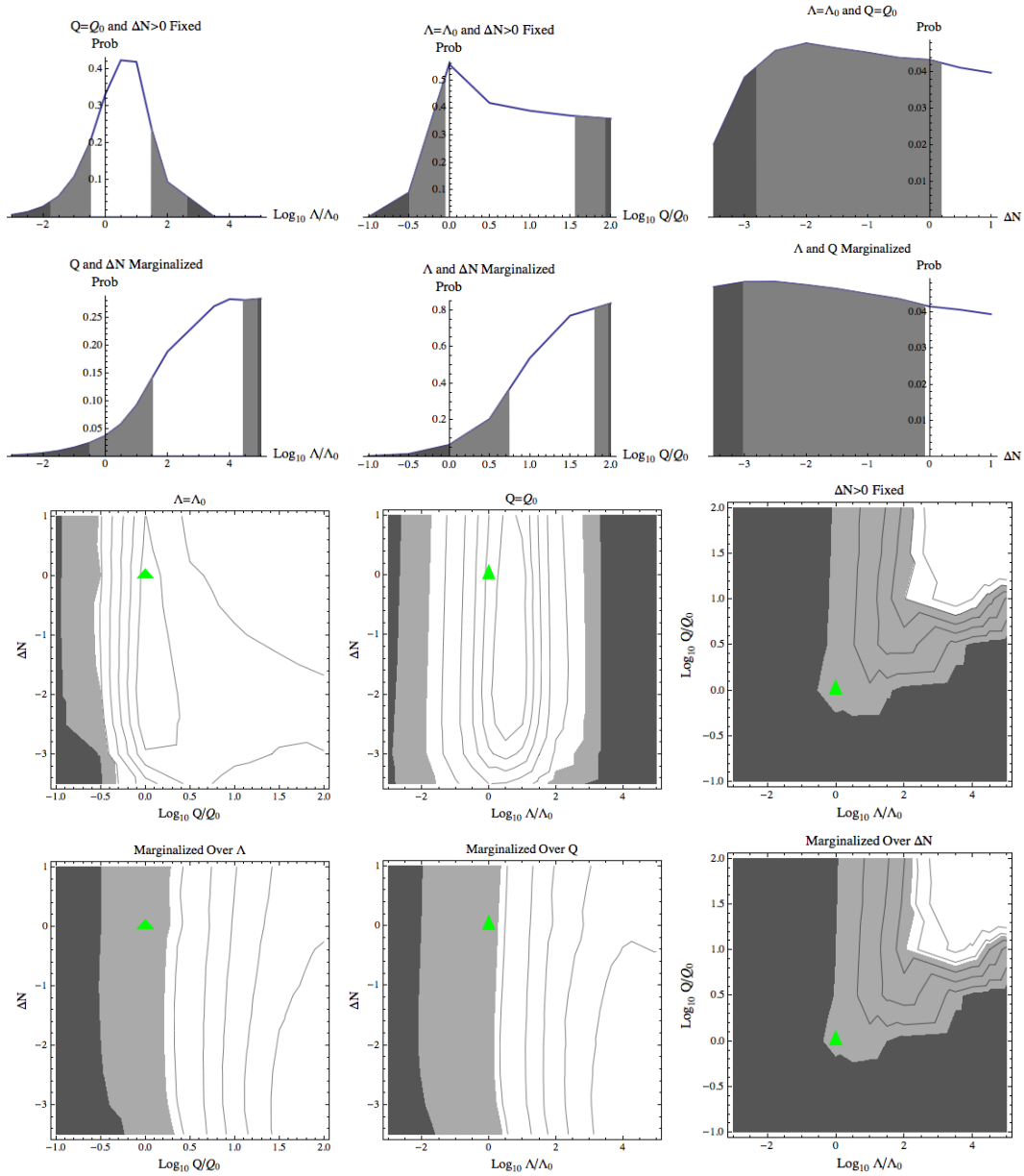


**Figure 2:**  $\Lambda > 0$ , Causal Diamond, Entropy Production. This is the only model studied which produces a peak in the  $Q$  distribution of the 2nd plot.

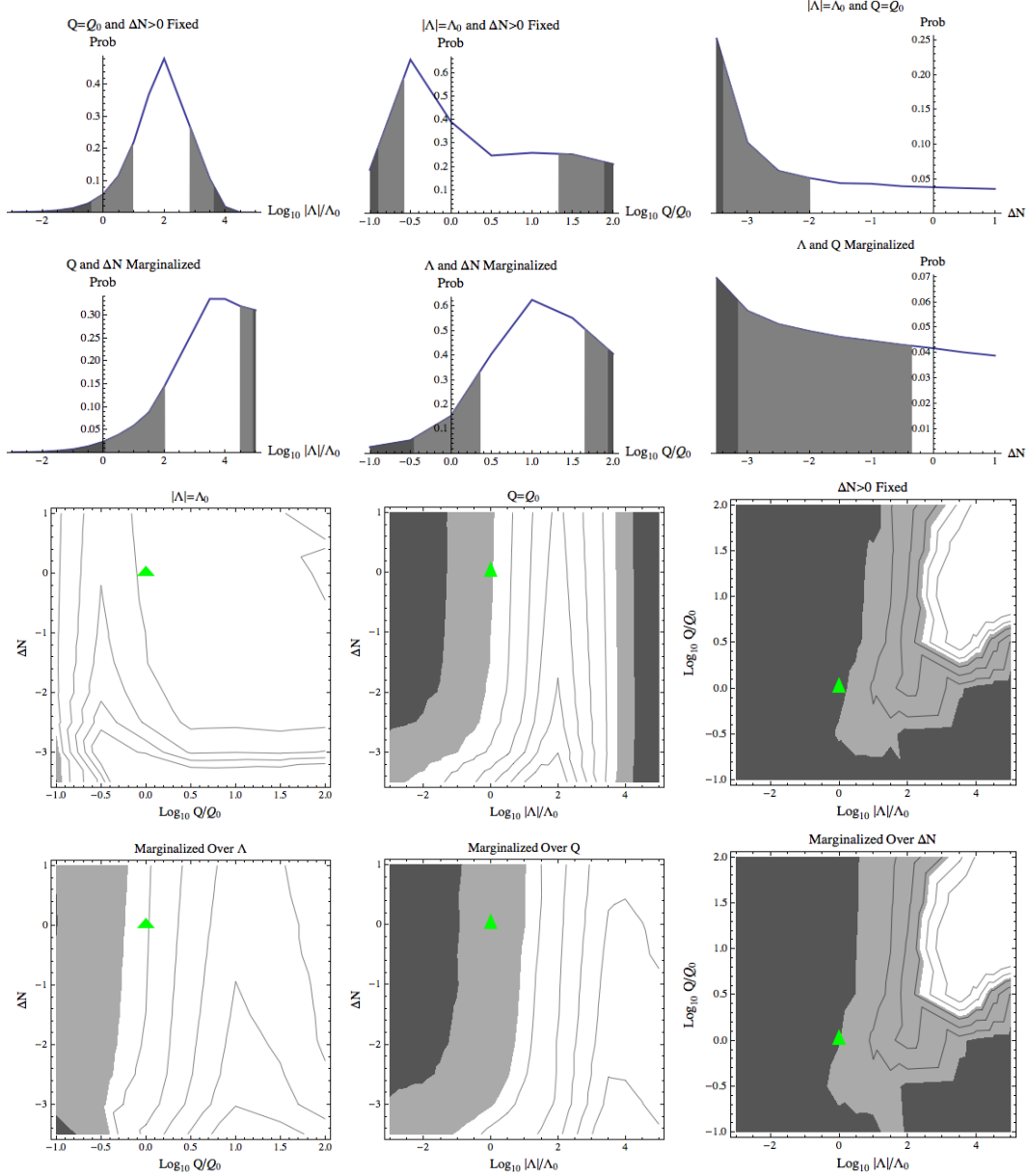


**Figure 3:**  $\Lambda < 0$ , Causal Diamond, Entropy Production. Unlike for  $\Lambda > 0$ , the probability density increases monotonically with curvature (3rd and 6th plot). However, the range allowed by observation ( $\Delta N > 0$ ) overlaps with the central  $1\sigma$  region (unshaded). This good agreement is not an artifact of our lower cut-off,  $\Delta N > 3.5$ , because the probability is about to be suppressed by the disruption of structure formation for slightly smaller  $\Delta N$ . This can be seen by studying the distribution over  $\Delta N$  at  $Q = 10^{-0.5}Q_0$  in the 7th and 10th plots.

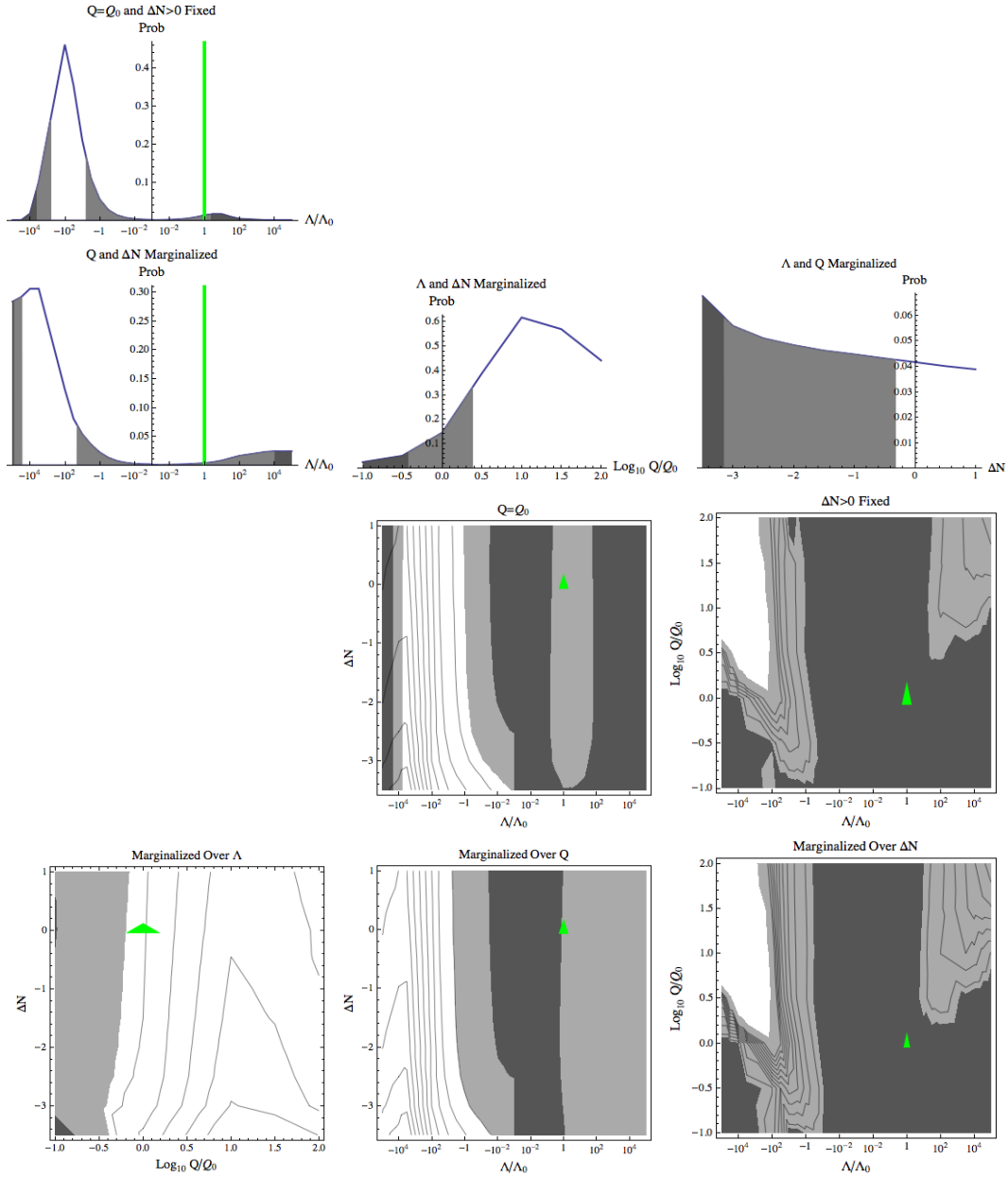


**Figure 4:** All values of  $\Lambda$ , Causal Diamond, Entropy Production.  $\Lambda < 0$  is preferred over  $\Lambda > 0$  by a factor of 25 (11) in the 1st (2nd) plot. The observed values of  $(\Lambda, Q)$  lie outside  $2\sigma$ , but within  $3\sigma$ , in the 6th and 9th plot.

## 4.2 Weighting by star formation + 5 Gyr in the causal diamond

For this choice of measure and observer model, we find that the observed values of parameters lie within or at the  $2\sigma$  contours of all plots with a single exception: in the bivariate distribution over  $Q$  and the full range of  $\Lambda$  (both positive and negative  $\Lambda$ ) with  $\Delta N$  marginalized (9th plot, Fig. 7), we find ourselves within  $3\sigma$ . The total probability for  $\Lambda < 0$  is 13 times larger than that for  $\Lambda > 0$  when  $Q$  and  $\Delta N$  are held fixed, and 12.6 times larger when  $Q$  and  $\Delta N$  are marginalized.

Unlike in the entropy production model shown previously, the distribution grows monotonically towards large  $Q$ , but not rapidly enough to render the observed value unlikely. The preferred positive value of  $\Lambda$  is virtually independent of  $Q$ , as explained in Sec. 5.5, and is roughly equal to the observed value, as seen in the 9th and 12th plot in Fig. 5.

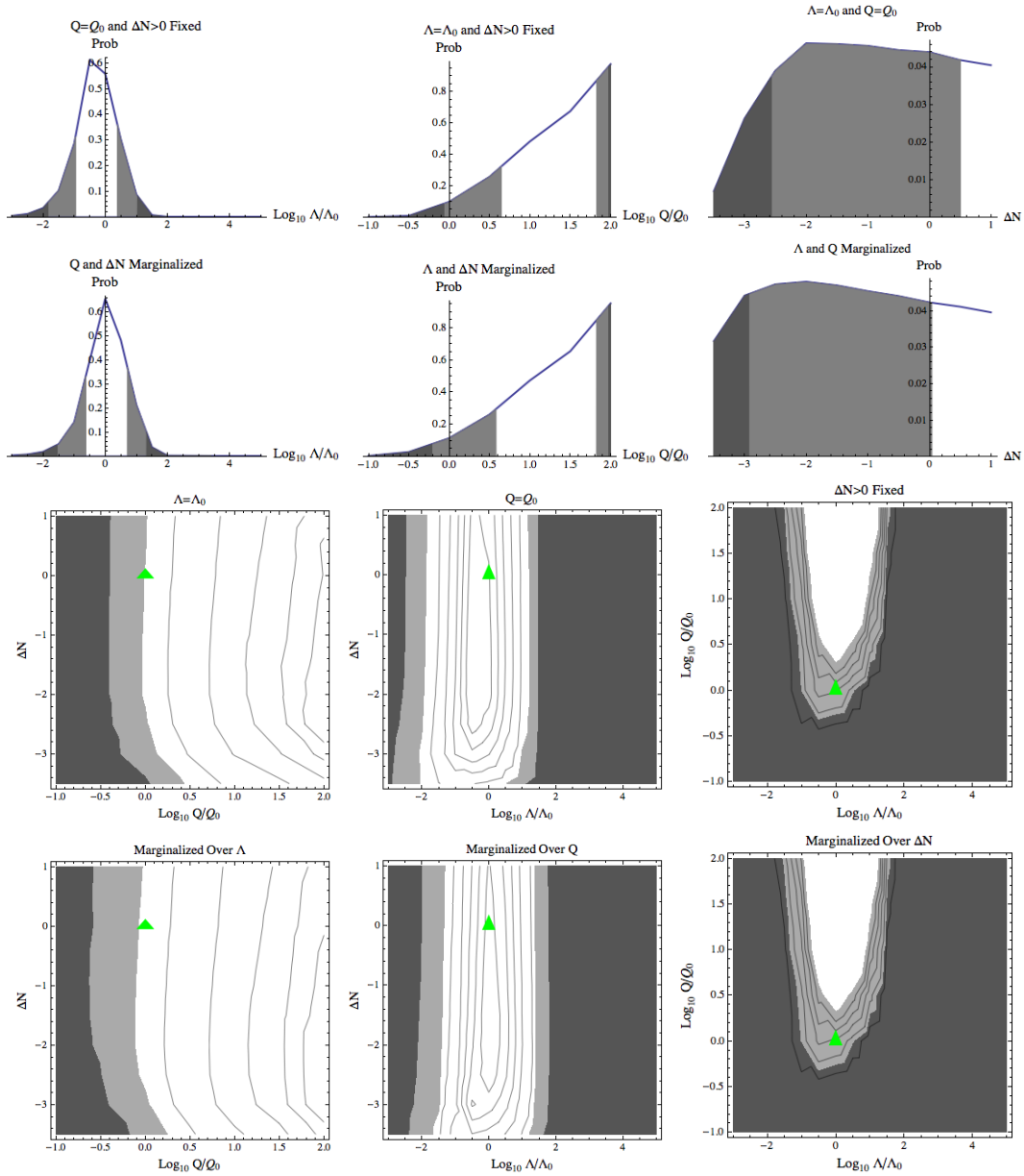


**Figure 5:**  $\Lambda > 0$ , Causal Diamond, 5 Gyr delay time. The preferred value of  $\Lambda$  is independent of  $Q$ , as seen in the 9th and 12th plots.

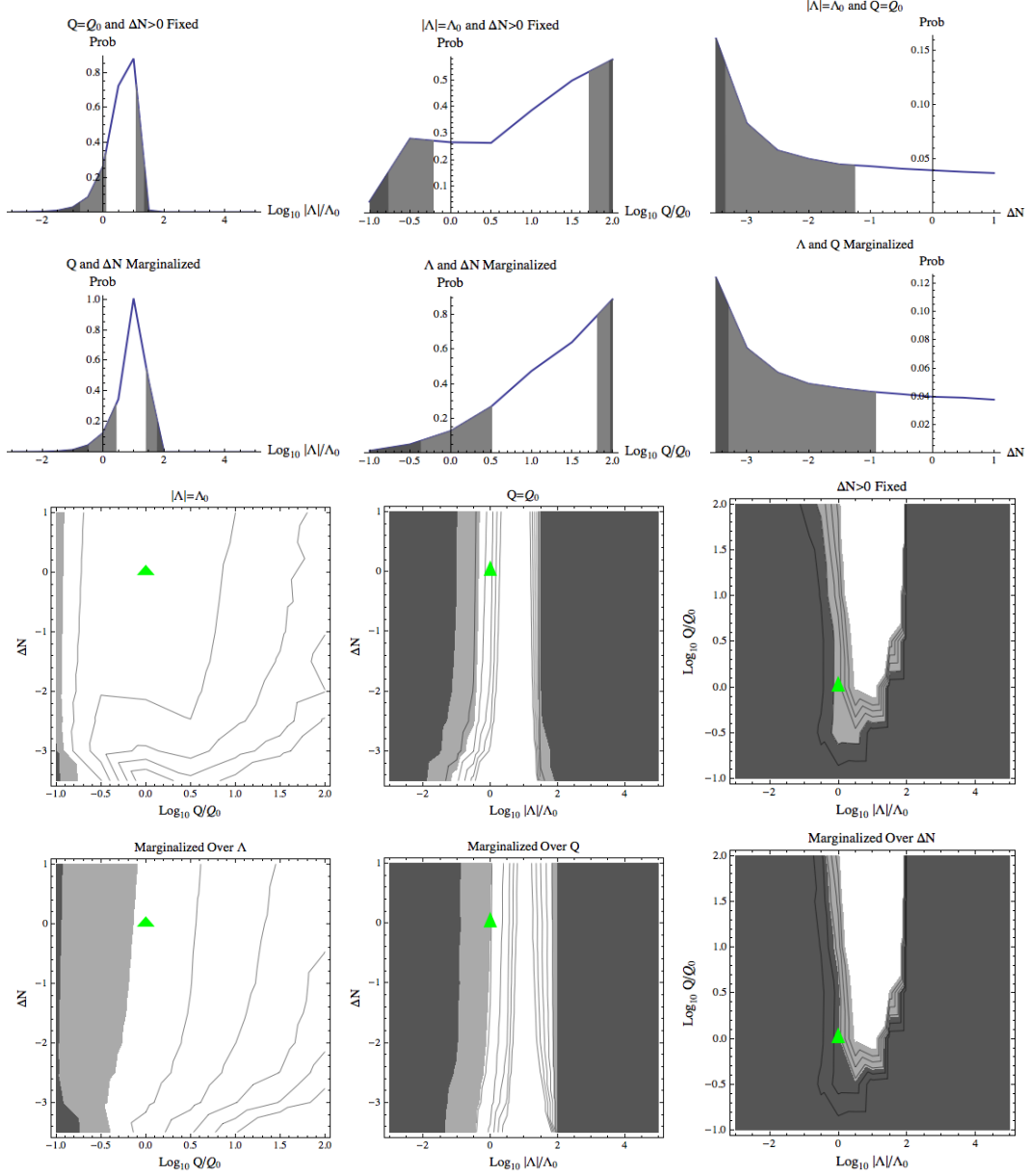


**Figure 6:**  $\Lambda < 0$ , Causal Diamond, 5 Gyr delay time. Note the peculiar feature around  $Q = Q_0$  in the 2nd plot. (It can also be seen in the 7th plot.) The increasing probability towards small  $\Delta N$  in the 3rd and 6th plot is not a runaway; see the caption of Fig. 3.

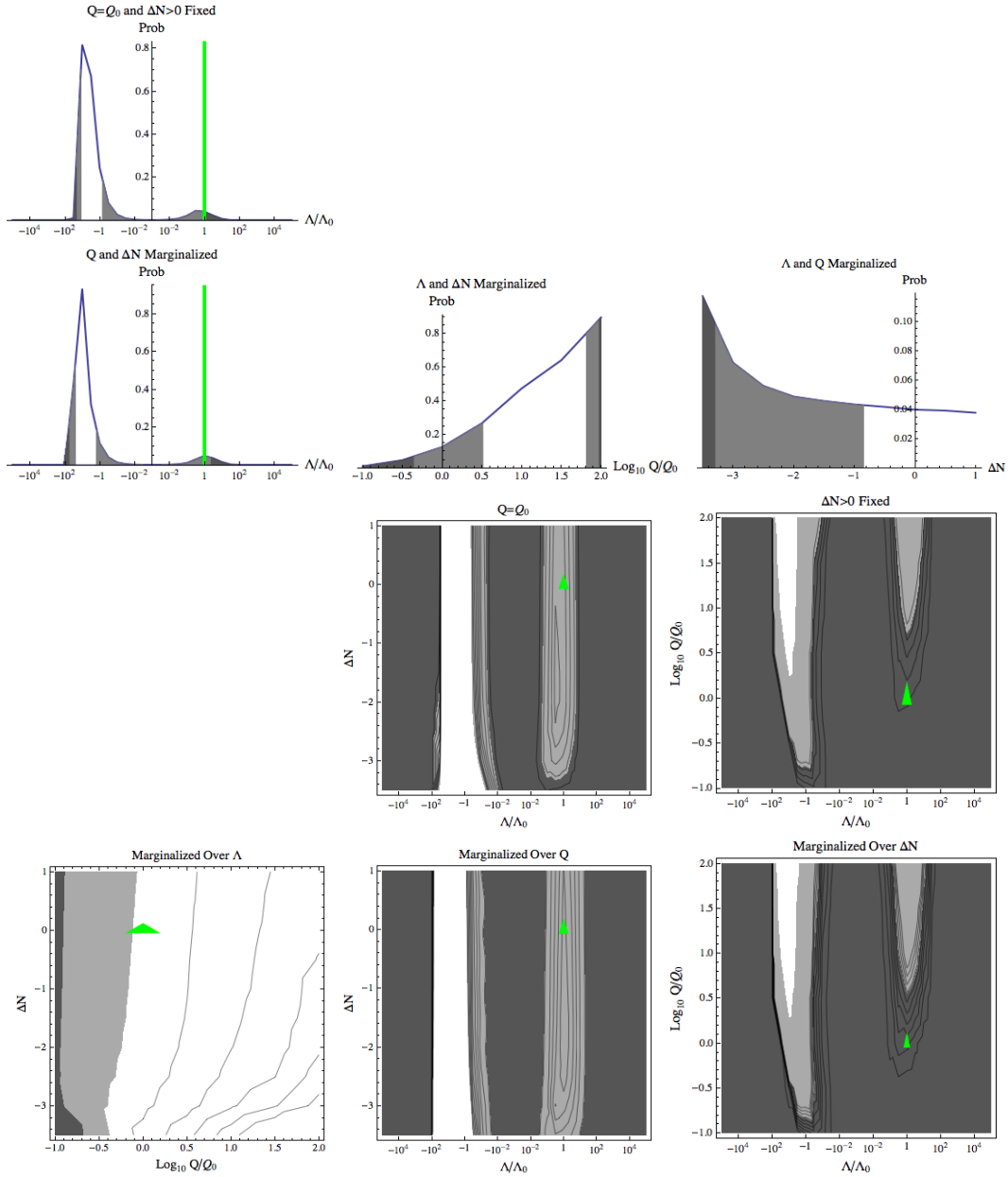


**Figure 7:** All values of  $\Lambda$ , Causal Diamond, 5 Gyr delay time. As with entropy production,  $\Lambda < 0$  is preferred over  $\Lambda > 0$  (here, by a factor of 13). The observed values of  $(\Lambda, Q)$  lie outside  $2\sigma$ , but within  $3\sigma$ , in the 6th and 9th plot.

### 4.3 Weighting by star formation + 10 Gyr in the causal diamond

The 10 Gyr delay model shares many features with the 5 Gyr delay model, with only small numerical differences. The preferred value of  $\Lambda$  is again nearly independent of  $Q$  but slightly smaller than with the 5 Gyr delay. This feature is explained in Sec. 5.5.

The observed values of parameters lie within or at the  $2\sigma$  contours of almost all plots. They are within  $3\sigma$  of some of the distributions that range over both positive and negative values of  $\Lambda$ . The total probability for negative  $\Lambda$  is 12.4 times larger than that for positive  $\Lambda$  when  $Q$  and  $\Delta N > 0$  are fixed, and 12.8 times larger when  $Q$  and  $\Delta N$  are marginalized.

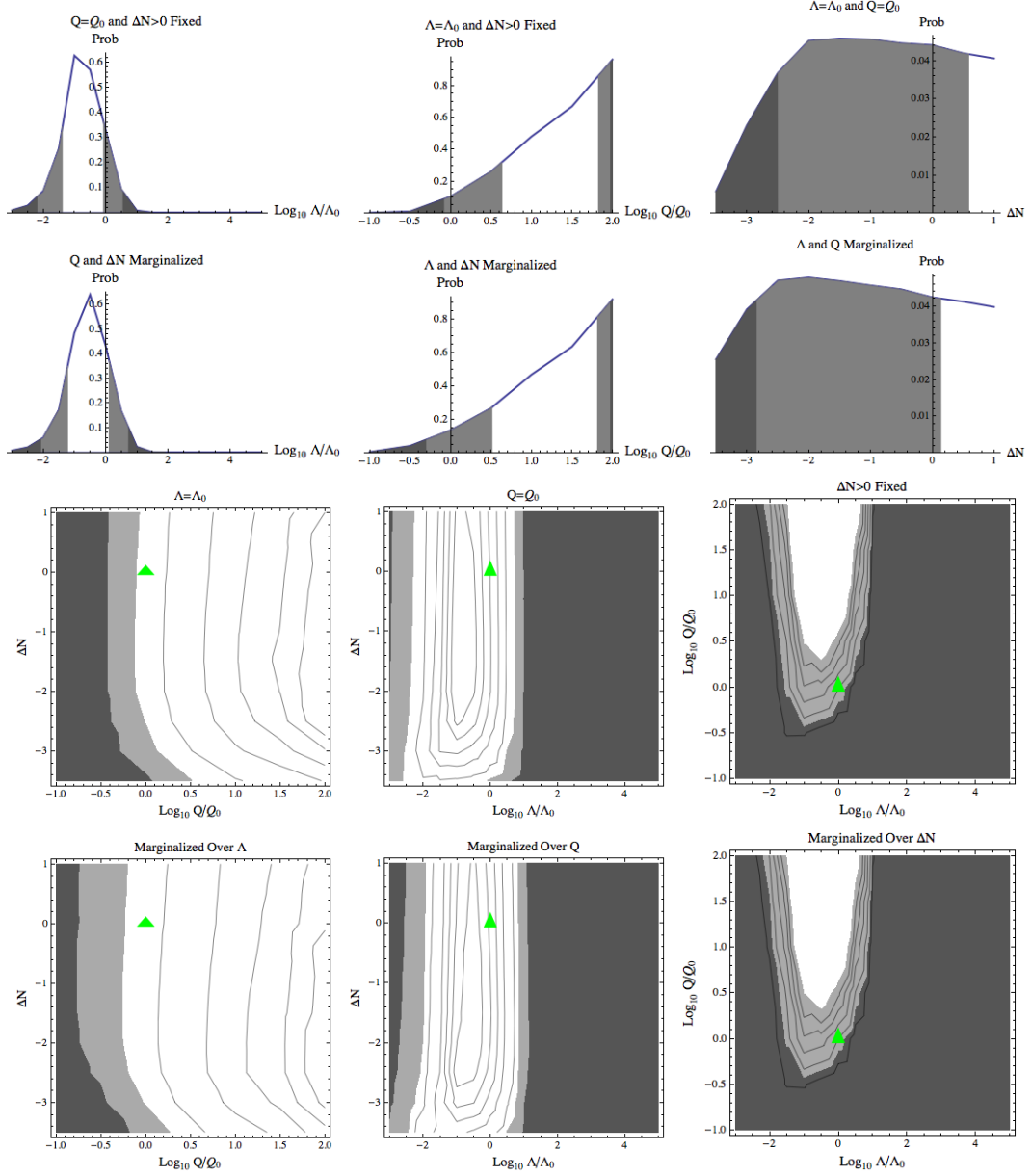


**Figure 8:**  $\Lambda > 0$ , Causal Diamond, 10 Gyr delay time. As with the 5 Gyr delay, we find a monotonic distribution over  $Q$  (2nd and 5th plot). The preferred value of  $\Lambda$  is independent of  $Q$ , and is somewhat smaller than with the 5 Gyr delay.

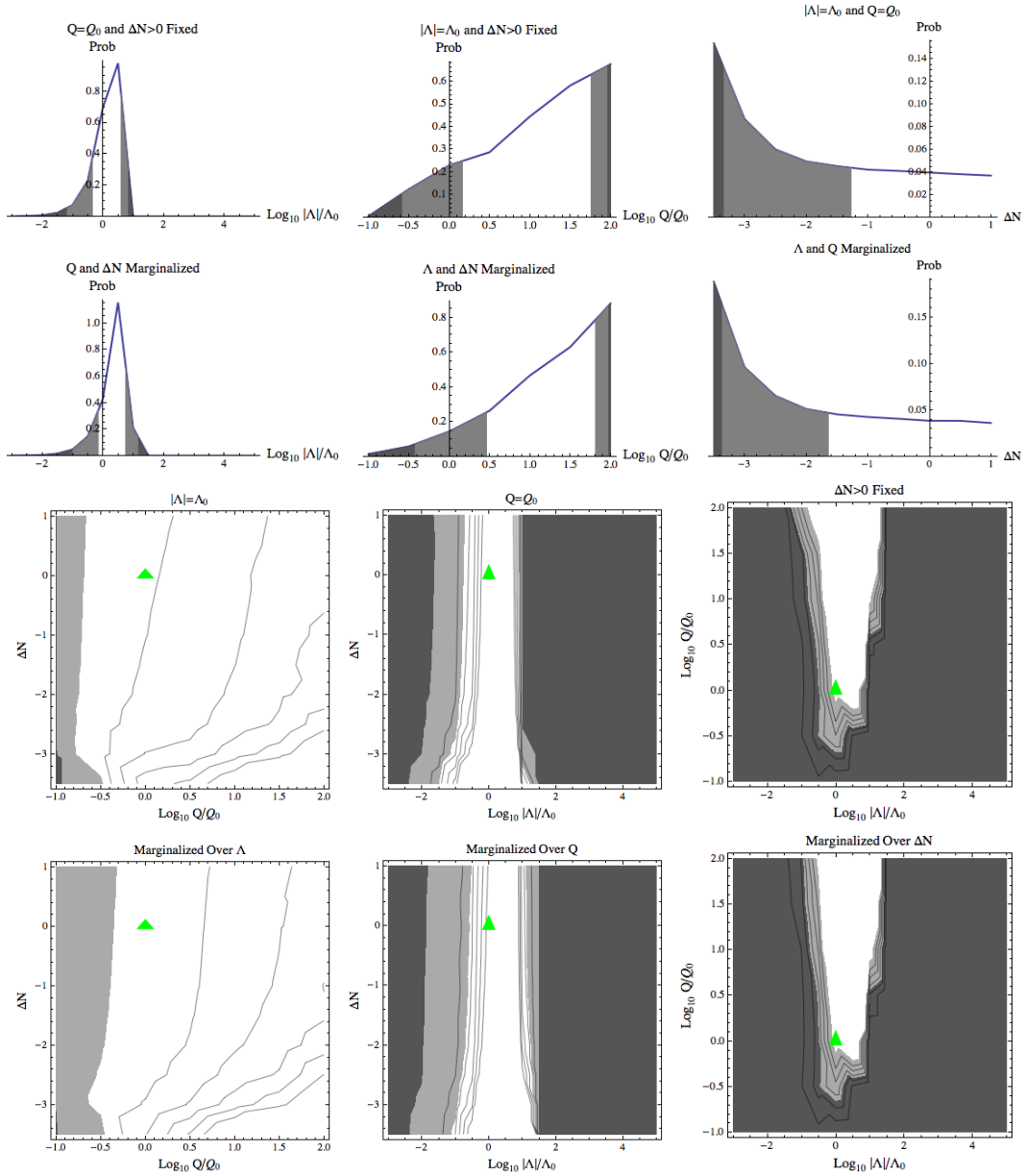


**Figure 9:**  $\Lambda < 0$ , Causal Diamond, 10 Gyr delay time. The 3rd and 6th plots show an increase in probability toward small  $\Delta N$ . This is not a runaway; see the caption of Fig. 3.

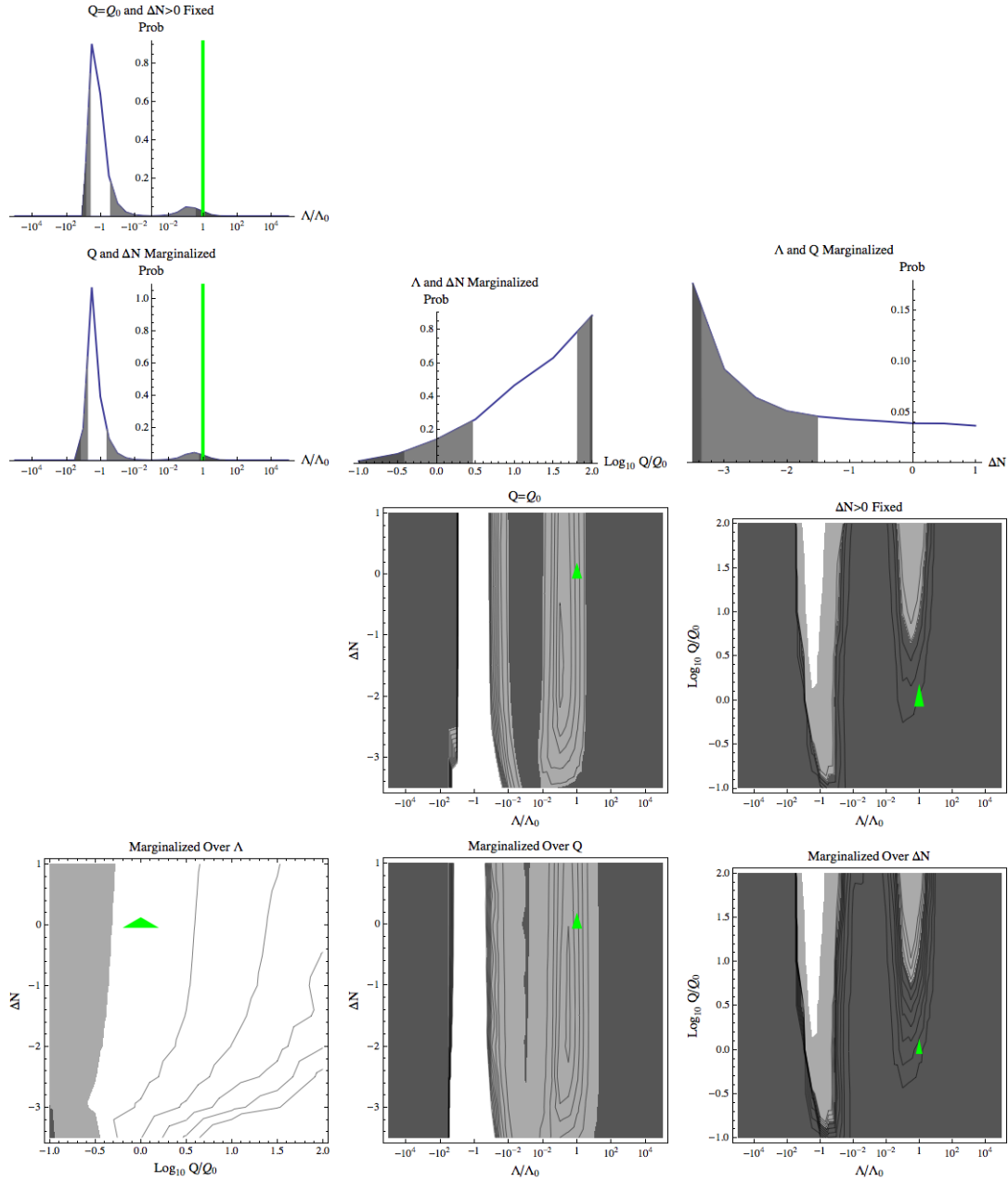


**Figure 10:** All values of  $\Lambda$ , Causal Diamond, 10 Gyr delay time. As usual,  $\Lambda < 0$  is more likely than  $\Lambda > 0$ . In the 9th and 12th plot, the observed values of  $(\Lambda, Q)$  lie outside  $2\sigma$  but within  $3\sigma$ .

#### 4.4 Weighting by entropy production in the causal patch

We now turn to the causal patch measure. Independently of the observer model, for  $\Lambda < 0$ , the rapid divergence as  $|\Lambda| \rightarrow 0$  (Sec. 5.3) prevents us from displaying confidence regions in the affected plots in Figs. 12, 15, and 18. For  $\Lambda > 0$ , the probability density over  $\log_{10}(|\Lambda|/\Lambda_0)$  goes to a constant for  $\Lambda \ll t_c^{-2}$ . This runaway is mild enough that we display confidence regions (based, as always, on an assumed cut-off at the end of our parameter range) in the relevant plots in Figs. 11, 14, and 17. The runaway is not always readily apparent but we have indicated all runaway directions with arrows. For  $\Lambda < 0$ , the growth towards small  $\Delta N$  (also described in Sec. 5.3) is so rapid at  $\Delta N = -3.5$  (the lower end of our parameter space) that confidence regions are very sensitive to the exact position of this cut-off and are not displayed.

In this subsection, we begin with the case where observers are modelled by entropy production. For  $\Lambda > 0$ , we find that the observed values are at or within  $2\sigma$ , except in those distributions which are susceptible to the above runaway towards small  $\Lambda$ . For  $\Lambda < 0$ , the only acceptable results obtain when curvature is fixed and negligible. Even in the absence of curvature, with  $\Delta N$  and  $Q$  fixed, negative values of the cosmological constant are more probable than positive values, by a factor of order 10. (As explained in Sec. 5.1, the distribution in  $\Lambda$  is wider than in the causal diamond case and so has significant support at the boundary of our parameter space. Thus, computing a more precise value of the relative probability for different signs of  $\Lambda$ , from our data alone, would not be very informative.)

Unlike the case of the causal diamond with the same observer model, the distribution in  $Q$  is monotonically increasing for  $\Lambda = \Lambda_0$  and  $\Delta N > 0$ . This difference is explained in Sec. 5.4. Like in the case of the causal diamond, the preferred value of  $\Lambda$  grows with  $Q$  (see Sec. 5.5).

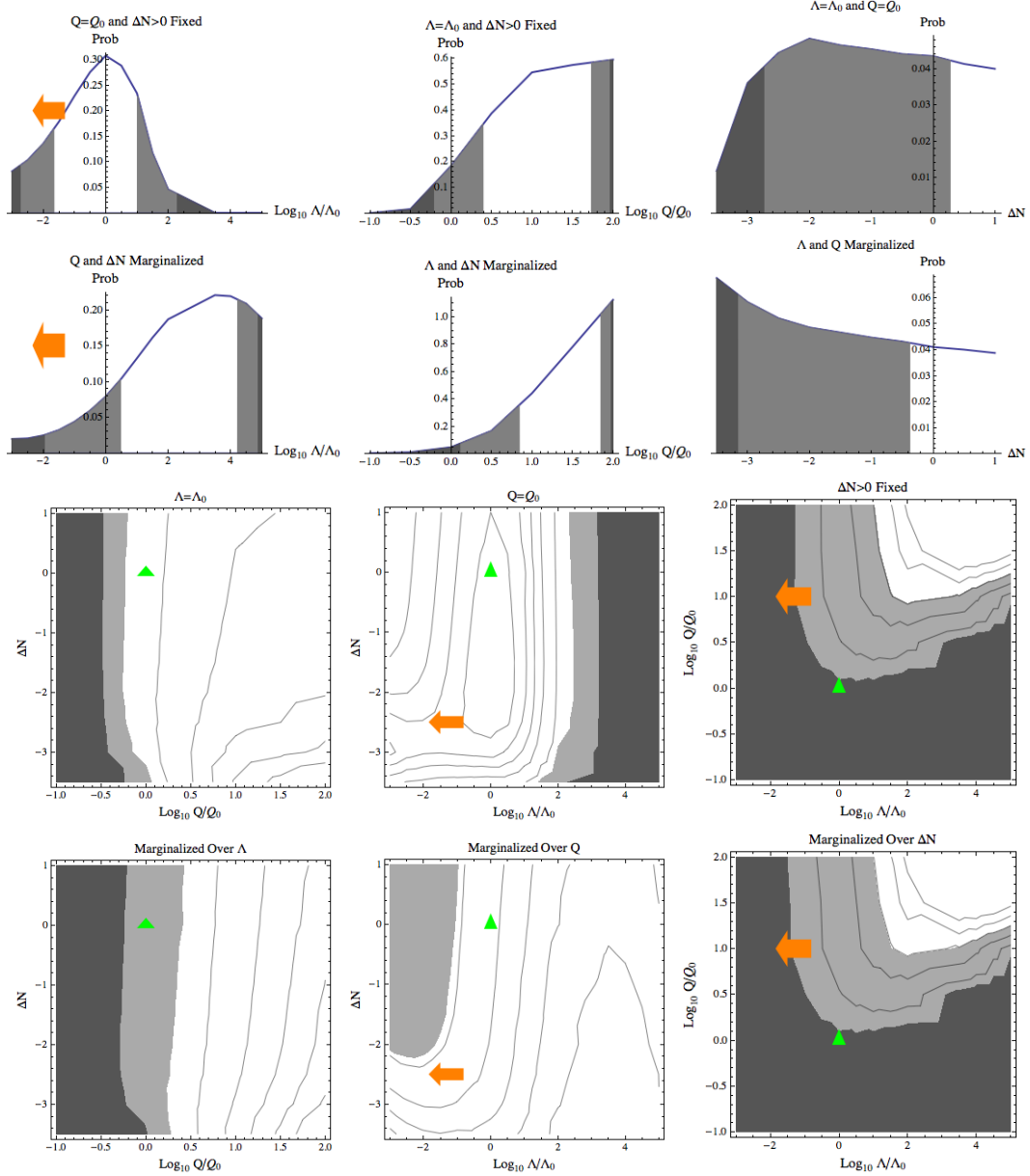


**Figure 11:**  $\Lambda > 0$ , Causal Patch, Entropy Production. The probability density goes to a constant for  $\Lambda \ll t_c^{-2}$ . This runaway is indicated by arrows. With  $\Delta N > 0$ , curvature dominates so late that the runaway is not evident even at the smallest values of  $\Lambda$  in the first plot. In the 8th and 11th plot, however, the distribution can be seen to flatten out towards small  $\Lambda$  at  $\Delta N = -3$ .

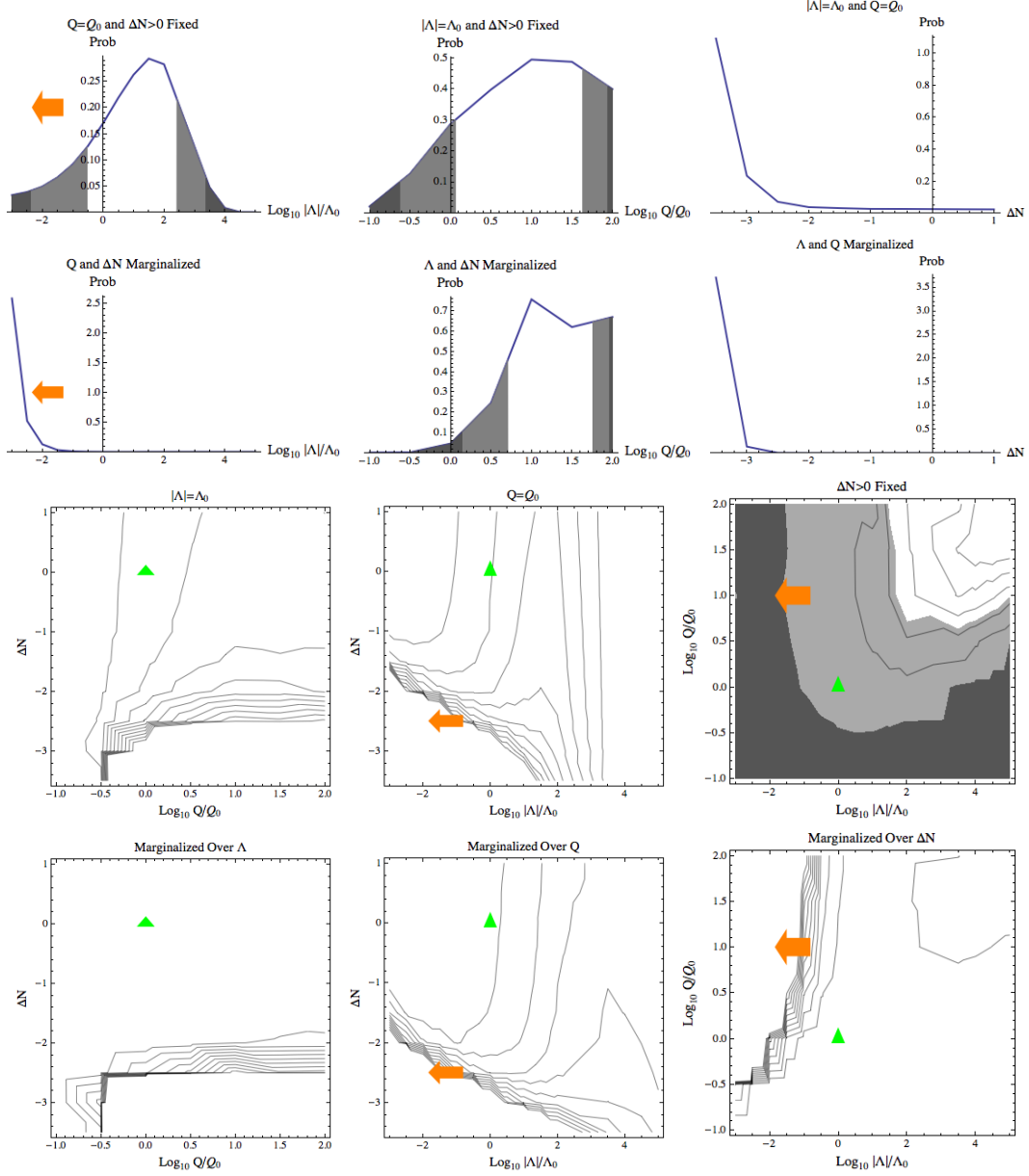


**Figure 12:**  $\Lambda < 0$ , Causal Patch, Entropy Production. The probability density grows like  $|\Lambda|^{-1}$  for  $\Lambda \ll t_c^{-2}$ . This runaway is indicated by arrows. At fixed  $\Lambda$ , small  $\Delta N$  is strongly preferred (3rd and 7th plots).

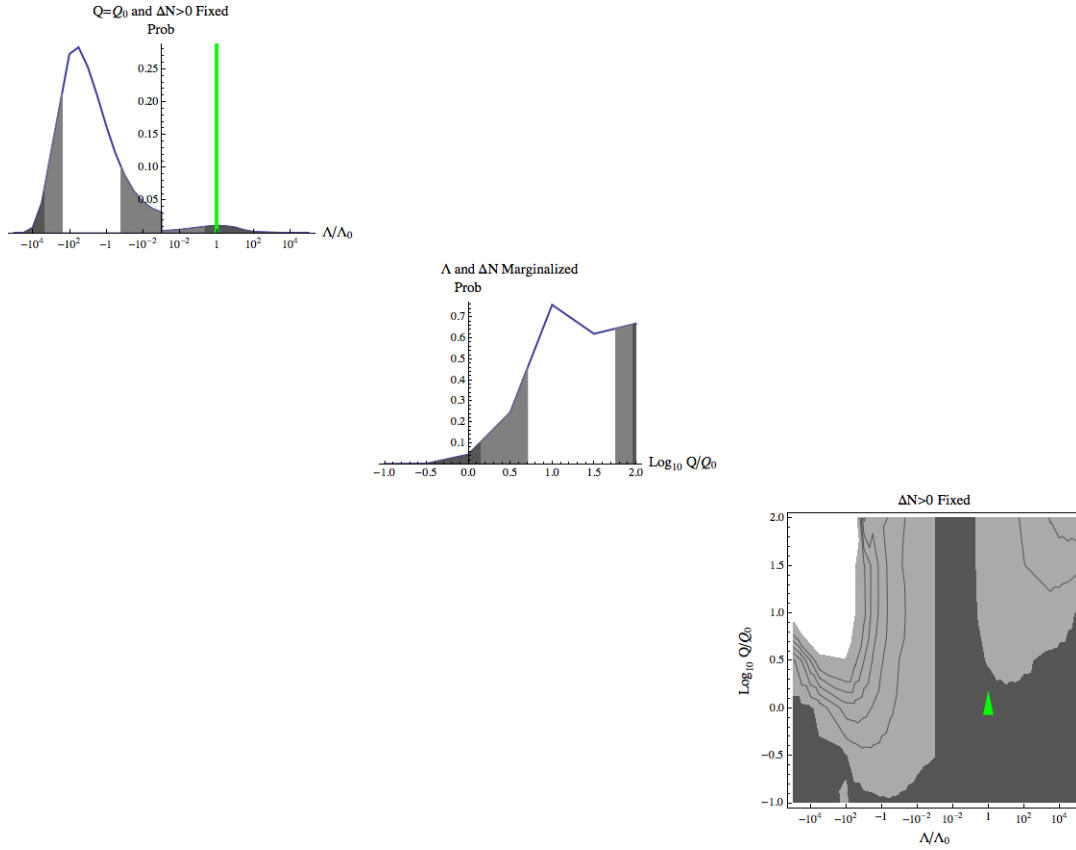


**Figure 13:** All values of  $\Lambda$ , Causal Patch, Entropy Production. In the presence of curvature,  $\Lambda < 0$  is preferred over  $\Lambda > 0$  by an arbitrarily large amount, depending on the cut-off in  $\Lambda$ . In the 5th plot, the observed value of  $(\Lambda, Q)$  lies outside  $2\sigma$ , but within  $3\sigma$ .

#### 4.5 Weighting by star formation + 5 Gyr in the causal patch

This case is very similar to the previous subsection, and we refer the reader to its text and captions.

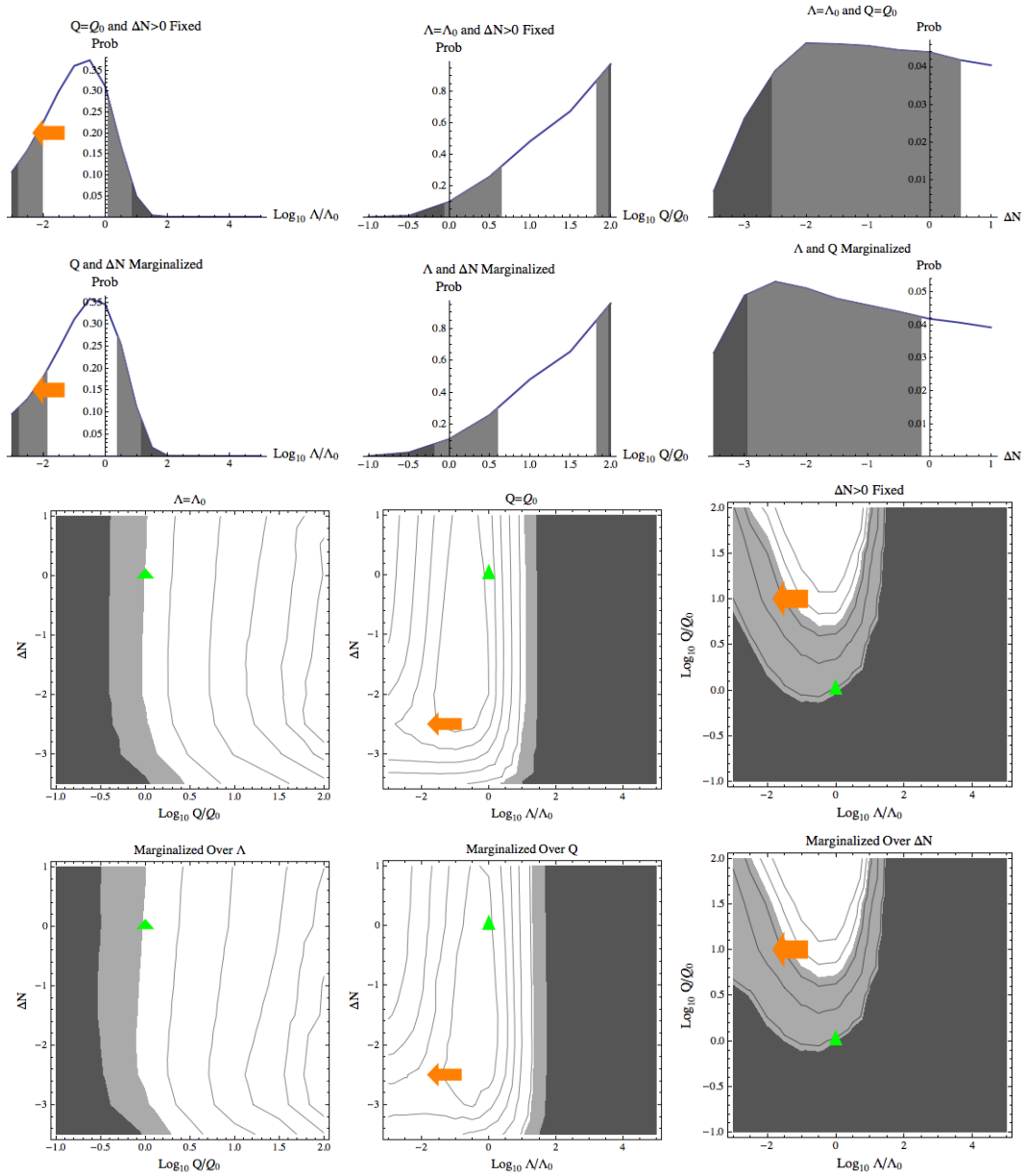


**Figure 14:**  $\Lambda > 0$ , Causal Patch, 5 Gyr delay time. In the absence of curvature, the preferred value of  $\Lambda$  is independent of  $Q$ , as seen in the 9th plot. For other comments, see the caption of Fig. 11.

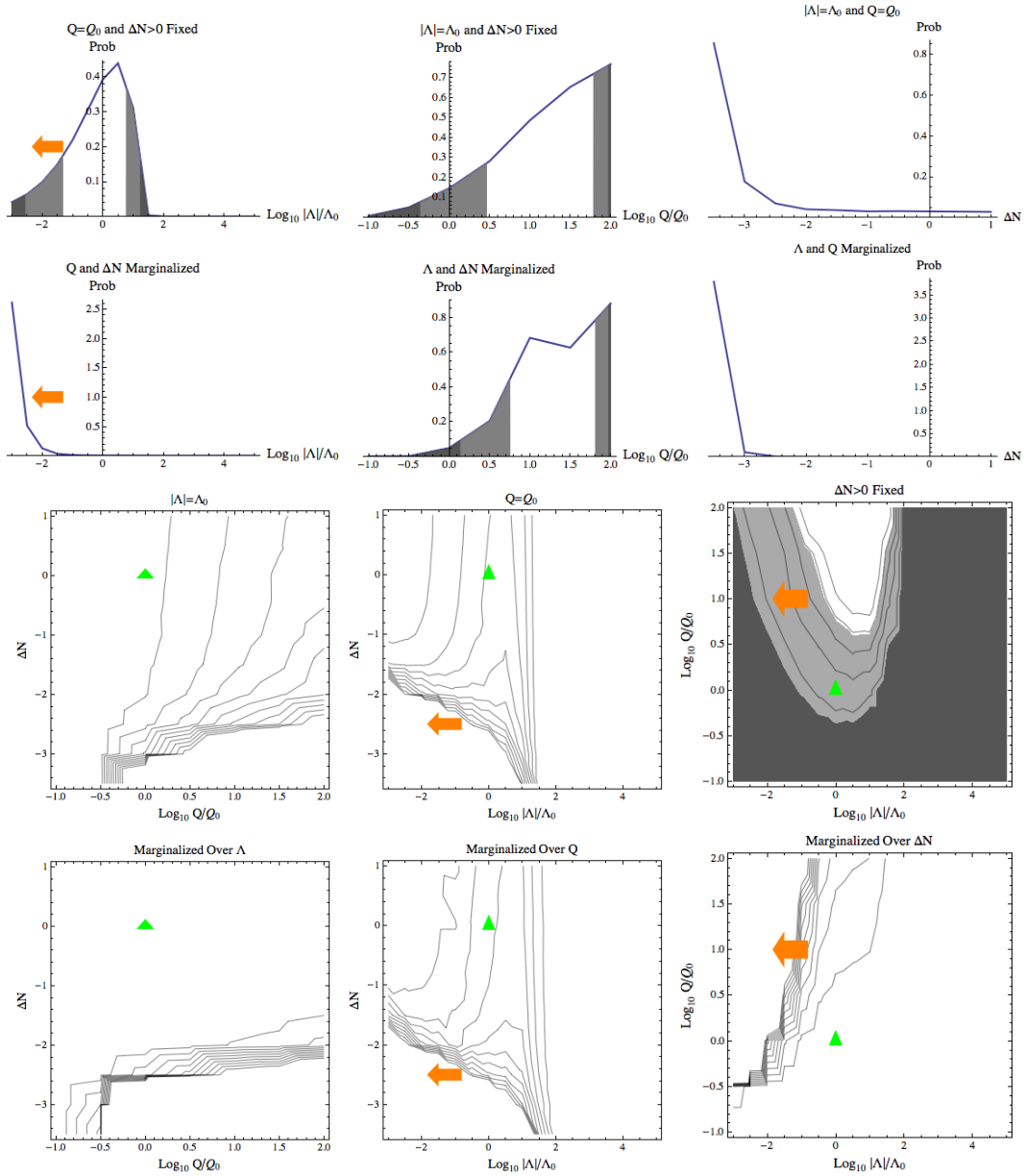


**Figure 15:**  $\Lambda < 0$ , Causal Patch, 5 Gyr delay time. In the absence of curvature, the preferred value of  $\Lambda$  is independent of  $Q$ , as seen in the 9th plot. For other comments, see the caption of Fig. 12.

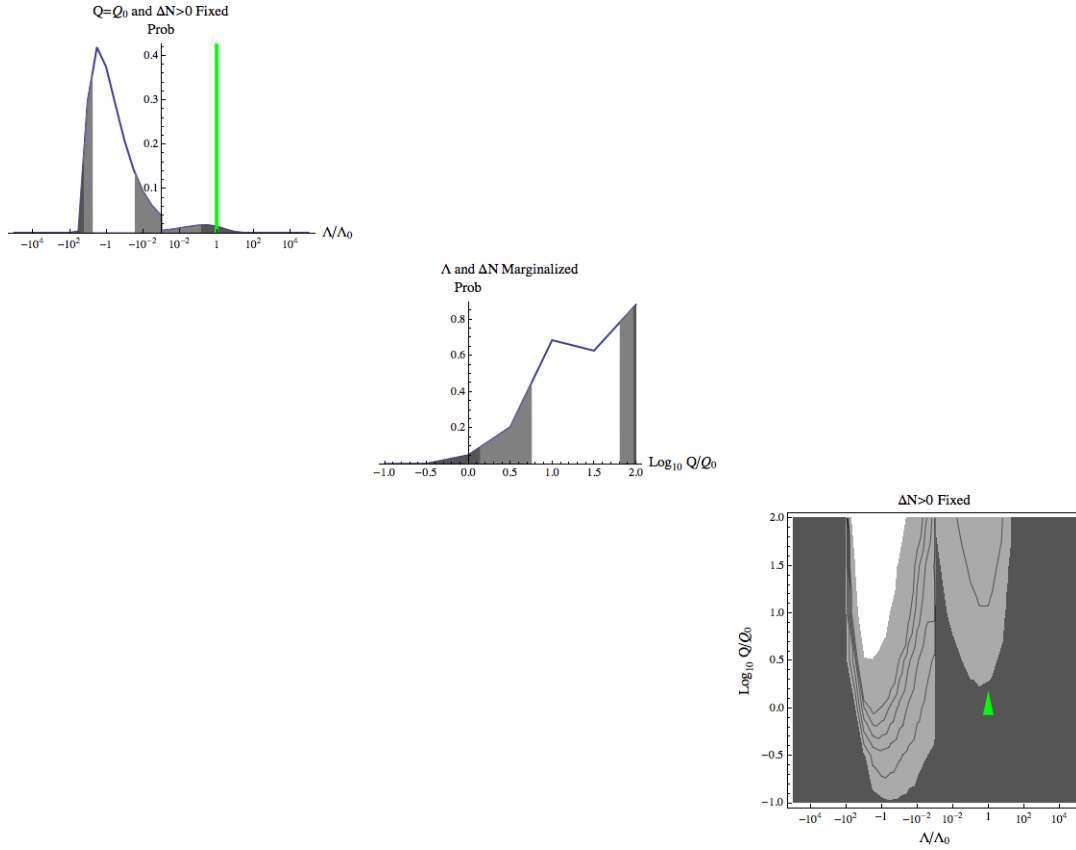


**Figure 16:** All Values of  $\Lambda$ , Causal Patch, 5 Gyr delay time. Negative  $\Lambda$  is preferred here by a factor of order 10 when curvature is absent. In the 5th plot, the data point is within  $3\sigma$ . For other comments, see the caption of Fig. 13.

#### 4.6 Weighting by star formation + 10 Gyr in the causal patch

This case is very similar to the previous subsection, and we refer the reader to its text and captions.

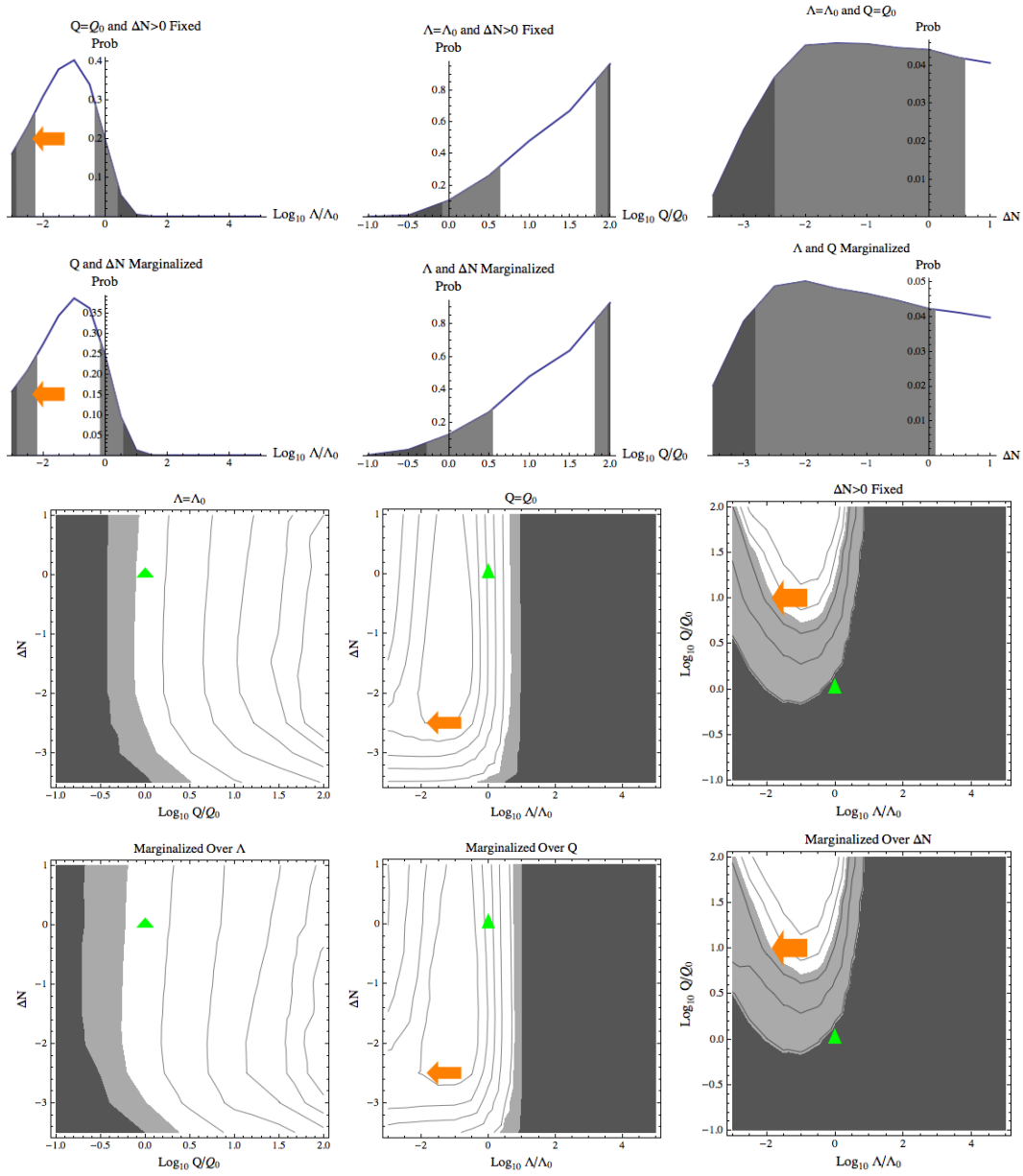


Figure 17:  $\Lambda > 0$ , Causal Patch, 10 Gyr delay time. See caption of Fig. 14.

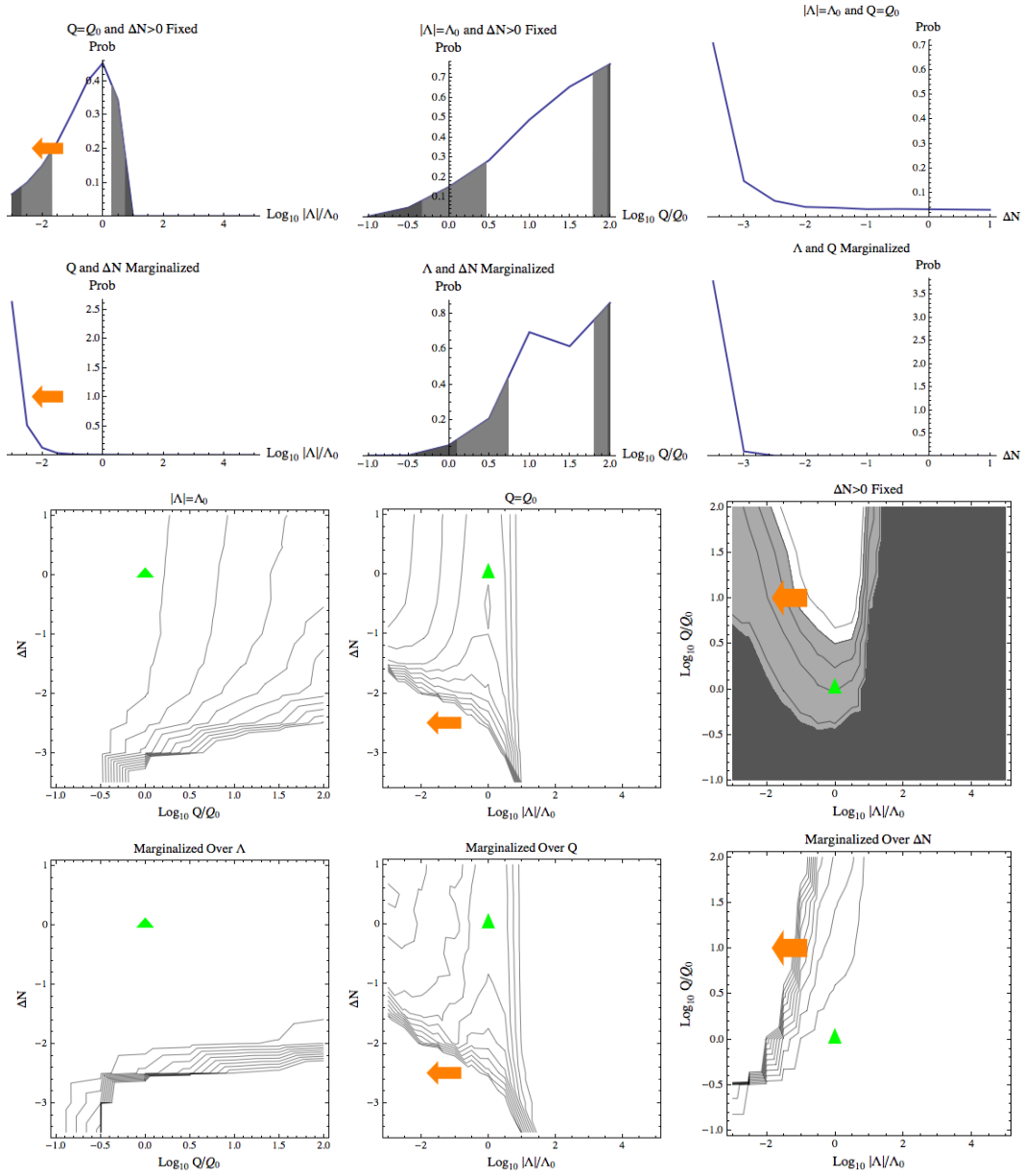
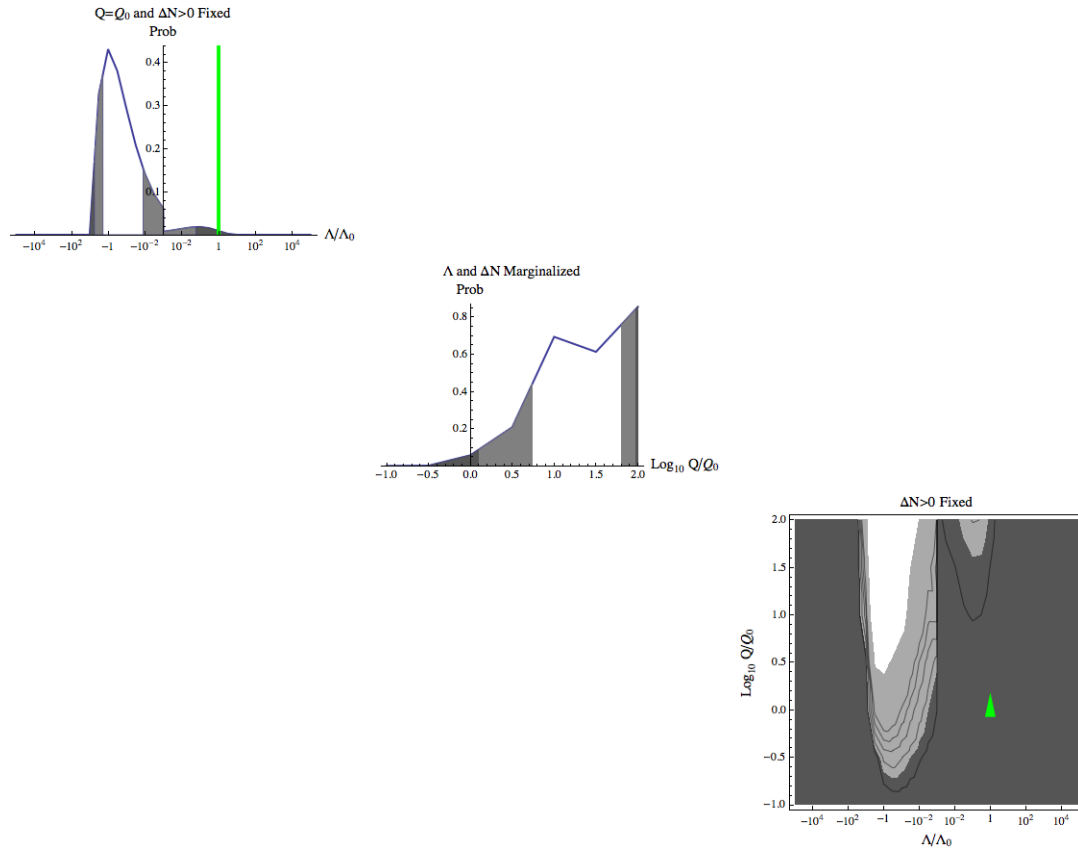


Figure 18:  $\Lambda < 0$ , Causal Patch, 10 Gyr delay time. See caption of Fig. 15.



**Figure 19:** All Values of  $\Lambda$ , Causal Patch, 10 Gyr delay time. See caption of Fig. 16.

## 5. Discussion

The main purpose of this section is to provide an intuitive qualitative understanding of the most important features in the plots of Sec. 4. We will also supply some additional quantitative results that are not immediately apparent in the plots. (In particular, we will compute the probability that nonvanishing spatial curvature will be detected in the near future, at the end of subsection 5.2.)

What are the physical consequences of varying the parameters  $(\Lambda, Q, \Delta N)$ ? Varying  $\Lambda$  or  $\Delta N$  changes both the dynamical evolution, and the geometry of the cut-off region. Dynamically, these parameters affect the rates of star formation and entropy production. Geometrically, they affect the amount of comoving volume contained within the causal patch or the causal diamond. In several probability distributions, the geometric effect is quantitatively more important than the dynamical effect.

The parameter  $Q$ , on the other hand, enters the probability distribution only dynamically, through its effects on the rate at which observers form. In an approximately homogeneous universe, the initial strength of density perturbations does not have an important effect on the comoving volume within the patch or diamond. (Ref. [32] discusses possible effects of the breakdown of the homogeneous approximation, which are not modeled here.)

### 5.1 Varying the cosmological constant only

Let us begin by discussing the probability distribution over the cosmological constant alone, with both remaining parameters fixed to their observed values. Its effects on star formation and on the geometry of the causal patch or diamond depend strongly on the sign of the cosmological constant. We begin by discussing the case  $\Lambda > 0$ ; our treatment follows Ref. [23].

With  $\Lambda > 0$ , structure formation, and thus star formation, halts after a time of order

$$t_\Lambda \equiv (3/\Lambda)^{1/2} . \tag{5.1}$$

However, this effect becomes important only for relatively large values of  $\Lambda$  of order  $100\Lambda_0$ . As we shall now see, these values are already suppressed by geometric effects. We will self-consistently treat the rate of observation,  $\dot{n}_{\text{obs}}(t)$ , as fixed. (We emphasize that this approximation, like all others in this section, is made for the sole purpose of elucidating our plots, which are always obtained using a full numerical calculation of both the geometry and the observation rate.)

For  $\Lambda > 0$ , a period of matter domination is succeeded, around the time  $t_\Lambda$ , by an infinite period of vacuum domination. In the sudden transition approximation, the

scale factor is given by

$$a(t) \propto \begin{cases} t^{2/3} & \text{if } t < \frac{2}{3}t_\Lambda , \\ \left(\frac{2}{3}t_\Lambda\right)^{2/3} \exp(t/t_\Lambda - 2/3) & \text{if } t \geq \frac{2}{3}t_\Lambda . \end{cases} \quad (5.2)$$

Matching both the scale factor and its derivative requires cumbersome shift terms, or order-one corrections to the matching time, like the  $2/3$  appearing in the above equation. Our goal is only to understand the rough features of our plots, not to keep track of all factors of order one. For this purpose, it suffices to match the value of the scale factor but not its derivative at the transition time. We will do so in all formulas below. For the present case, the simplified version of the scale factor is

$$a(t) \propto \begin{cases} t^{2/3} & \text{if } t < t_\Lambda , \\ t_\Lambda^{2/3} \exp(t/t_\Lambda - 1) & \text{if } t \geq t_\Lambda . \end{cases} \quad (5.3)$$

By Eq. (2.2), the comoving radius of the causal patch is given by

$$\chi_{\text{patch}}(t) \propto \begin{cases} 4t_\Lambda^{1/3} - 3t^{1/3} & \text{if } t < t_\Lambda , \\ t_\Lambda^{1/3} \exp(-t/t_\Lambda + 1) & \text{if } t \geq t_\Lambda . \end{cases} \quad (5.4)$$

By Eq. (2.3), the comoving radius of the causal diamond is given by

$$\chi_{\text{dia}}(t) \propto \begin{cases} 3t^{1/3} & \text{if } t \ll t_\Lambda , \\ t_\Lambda^{1/3} \exp(-t/t_\Lambda + 1) & \text{if } t \gg t_\Lambda . \end{cases} \quad (5.5)$$

The “edge” of the causal diamond, where the future light-cone from the reheating surface meets intersects the boundary of the causal patch, occurs at the time  $0.23t_\Lambda$  [23]. Since this is approximately the same time at which the scale factor changes from power law to exponential growth, there is no need for another case distinction in Eq. (5.16) at this level of approximation.

Since in this section we are assuming negligible spatial curvature, the comoving volume for the patch is

$$V_c^{\text{patch}}(t) \propto \begin{cases} \frac{4\pi}{3} (4t_\Lambda^{1/3} - 3t^{1/3})^3 & \text{if } t < t_\Lambda , \\ \frac{4\pi}{3} t_\Lambda \exp(-3t/t_\Lambda + 3) & \text{if } t \geq t_\Lambda . \end{cases} \quad (5.6)$$

while that for the diamond is

$$V_c^{\text{dia}}(t) \propto \begin{cases} 36\pi t & \text{if } t \ll t_\Lambda , \\ \frac{4\pi}{3} t_\Lambda \exp(-3t/t_\Lambda + 3) & \text{if } t \gg t_\Lambda . \end{cases} \quad (5.7)$$

Now we are in a position to derive a probability distribution for  $\Lambda$  by counting observers:

$$\frac{dp}{d\log_{10}\Lambda} \propto \frac{d\tilde{p}}{d\log_{10}\Lambda} \times \int dt \dot{n}_{\text{obs}}(t) V_c(t) \quad (5.8)$$

Recall from section 2.2 that we assume  $d\tilde{p}/d\log_{10}\Lambda \propto \Lambda$ , and that here we are assuming  $\dot{n}_{\text{obs}}(t)$  is independent of  $\Lambda$ .

Beginning with the *causal diamond*, we see that

$$\frac{dp}{d\log_{10}\Lambda} \propto \Lambda \left[ 36\pi \int_0^{t_\Lambda} dt \dot{n}_{\text{obs}}(t)t + \frac{4\pi}{3} t_\Lambda \int_{t_\Lambda}^\infty dt \dot{n}_{\text{obs}}(t) \exp(-3t/t_\Lambda + 3) \right]. \quad (5.9)$$

If  $\dot{n}_{\text{obs}}(t)$  were constant in time, the bracketed terms would be proportional to  $t_\Lambda^2 \propto \Lambda^{-1}$  and we would obtain a distribution flat in  $\log_{10}\Lambda$ . In reality,  $\dot{n}_{\text{obs}}(t)$  has a peak at a time  $t_{\text{peak}}$  of order Gyr with a width that is also of order Gyr. This will serve to select a preferred value of  $\Lambda$  as follows. If  $t_\Lambda \ll t_{\text{peak}}$ , then only the second integral in Eq. (5.9) contributes, and this integral features an exponential suppression due to the rapid emptying of the de Sitter horizon during  $\Lambda$ -domination. If  $t_\Lambda \gg t_{\text{peak}}$ , then only the first integral contributes, and its contribution will be independent of  $\Lambda$ . But there are more vacua with larger  $\Lambda$  than smaller  $\Lambda$ ; this is encoded in the overall factor of  $\Lambda$  coming from the prior, which tend to push the probability toward larger values of  $\Lambda$ . Thus we conclude that the most favorable value of  $\Lambda$  is one where  $t_{\text{peak}} \approx t_\Lambda$  (more precisely we conclude that  $t_{\text{peak}} \approx t_{\text{edge}}$ , but these are the same up to order-one factors). Similarly, the width of our distribution depends on the width of  $\dot{n}_{\text{obs}}(t)$ : if  $t_{\text{on}}$  and  $t_{\text{off}}$  are the times when  $\dot{n}_{\text{obs}}(t)$  is at half-maximum, then the corresponding values of  $\Lambda$  will give the approximate  $1\sigma$  boundaries in the the  $\log_{10}\Lambda$  distribution [23].

The same analysis holds for the *causal patch*, with one modification. In Eq. (5.6), we see that for  $t < t_\Lambda$  the patch volume has some residual  $\Lambda$  dependence. So when  $t_{\text{peak}} \ll t_\Lambda$ , the factor of  $\Lambda$  from the prior is partially cancelled by the factor of  $t_\Lambda \sim \Lambda^{-1/2}$  in the comoving volume. The result is that the probability distributions using the patch are more tolerant of small values of  $\Lambda$  than those using the diamond.

These estimates are confirmed by our plots for the probability distribution over  $\Lambda > 0$ , with  $Q = Q_0$  and  $\Delta N > 0$  fixed (the first plot in each figure). Fig. 2 shows the result for entropy production, where the most likely value of  $\Lambda$  is about  $10\Lambda_0$ . This corresponds to  $t_{\text{peak}} \approx 2$  Gyr, so we expect that in the 5 Gyr delay time model of Fig. 5 the most likely value of  $\Lambda$  would be smaller by a factor of  $(2/7)^2 \approx .08$ , and indeed we can see in that plot that the most likely value is now slightly smaller than  $\Lambda_0$ . With a 10 Gyr time delay, our estimate says that most likely value of  $\Lambda$  should be  $(2/12)^2 \approx .03$  times that for entropy production, and in Fig. 8 we see that the most

likely value is down to nearly  $\Lambda_0/10$ . Also, for the patch, in Figs. 11, 14, and 17 we see a broadening of the distributions compared to those of the diamond.

The  $\Lambda < 0$  case has several important differences from the  $\Lambda > 0$  case. Instead of halting structure formation, a collapsing universe leads to a period of enhanced structure growth. However, the structures which grow during the collapse phase are much larger than the structures which grow in the early universe. The largest of these cannot cool and do not form stars. As a result, enhanced structure growth is actually a subdominant effect in explaining the difference between the probability distributions. Far more important is the difference in geometry for a  $\Lambda < 0$  universe, which we will now discuss.

The scale factor for  $\Lambda < 0$  (and negligible curvature) is

$$a(t) = \left[ \frac{2}{3} t_\Lambda \sin \left( \frac{3t}{2t_\Lambda} \right) \right]^{2/3}. \quad (5.10)$$

The comoving volume can be expressed in terms of hypergeometric functions. Once again the behavior of the *causal diamond* is easier to estimate. A reasonable approximation is

$$V_c^{\text{dia}}(t) \propto \begin{cases} 36\pi t & \text{if } t < \pi t_\Lambda/3, \\ 36\pi \left( \frac{2\pi}{3} t_\Lambda - t \right) & \text{if } t \geq \pi t_\Lambda/3. \end{cases} \quad (5.11)$$

For  $\Lambda < 0$ , the “edge” time for the causal diamond is  $t_{\text{edge}} = \pi t_\Lambda/3$  (coinciding with the turnaround time for the scale factor). Since  $\pi/3 > 0.23$ , the probability distribution for  $\Lambda < 0$  peaks at a value of  $|\Lambda|$  which is higher by a factor of  $(\pi/(3 \times 0.23))^2 \approx 21$  than that for  $\Lambda > 0$  with the same observer model. This is evident when comparing, for example, the first plot of Fig. 2 with that of Fig. 3. It is also manifest in the distributions over both positive and negative values of  $\Lambda$ , such as the first plot in Fig. 4.

According to our approximate equation, the diamond’s volume at  $t = t_{\text{edge}}$  should be larger for  $\Lambda < 0$ , by the same factor of 21, for equal  $|\Lambda|$ . Indeed, the first plot of Fig. 4 shows that height of the peak for  $\Lambda < 0$  is larger than for  $\Lambda > 0$  by about this amount. We can also compare the integrated probabilities for each sign of  $\Lambda$ ,  $p(\Lambda < 0)/p(\Lambda > 0)$ . For the entropy production model, this ratio is 25, which we can attribute to the enhancement of diamond volume for those universes with  $\Lambda < 0$  where  $t_{\text{edge}}$  coincides with the peak of entropy production. In the 5 Gyr and 10 Gyr time delay models the ratio is 13 and 12.4, respectively. The ratio is smaller than in the entropy model, because about half of the range of  $\log_{10} \Lambda$  has zero probability in the time delay models because those universes crunch before  $t = t_{\text{delay}}$ .

Similar conclusions hold for the *causal patch* when  $\Lambda < 0$ . As for  $\Lambda > 0$ , small values of  $|\Lambda|$  are less suppressed by the causal patch than by the diamond. This

broadens the probability distribution so much that our range of  $\log_{10} |\Lambda|$  misses some of the probability for small  $|\Lambda|$ , as one can see in the first plot of Figs. 12, 15, and 18. This means we cannot accurately compute certain quantities, such as the ratio  $p(\Lambda < 0)/p(\Lambda > 0)$ , for the patch. We can make some qualitative statements, though. For the entropy production model, we expect that the ratio should be of the same order for the patch as for the diamond. For the time delay models, the ratio should decrease for the same reason that it decreased in the diamond: the universe crunches too early in part of the parameter space. However, the decrease should be smaller in the patch than it was in the diamond. That is because the universes which are crunching “too early” are the ones with large  $|\Lambda|$ , but as discussed above this is precisely the region of parameter space which is relatively de-emphasized in the patch as compared with the diamond.

## 5.2 Varying spatial curvature only

Now we will consider the implications of varying spatial curvature, while keeping  $\Lambda$  (and  $Q$ ) fixed at its observed value (or at minus this value; see below). How is structure formation and observer formation affected by period of curvature domination following matter domination, beginning at  $t \sim t_c$ . In the sudden transition approximation, the scale factor is

$$a(t) = \begin{cases} t^{2/3} t_c^{1/3} & \text{if } t < t_c , \\ t & \text{if } t_c \leq t < t_\Lambda , \\ t_\Lambda \exp(t/t_\Lambda - 1) & \text{if } t_\Lambda \leq t . \end{cases} \quad (5.12)$$

By Eq. (2.2), the comoving radius of the causal patch is given by

$$\chi_{\text{patch}}(t) \propto \begin{cases} 4 - 3(t/t_c)^{1/3} + \ln \frac{t_\Lambda}{t_c} & \text{if } t < t_c , \\ 1 + \ln \frac{t_\Lambda}{t} & \text{if } t_c \leq t < t_\Lambda , \\ \exp(-t/t_\Lambda + 1) & \text{if } t_\Lambda \leq t . \end{cases} \quad (5.13)$$

To compute the radius of the diamond, we need to first find the edge time  $t_{\text{edge}}$  where the the forward and backward lightcones meet. We will assume (and later check for consistency), that this time is during the period of curvature domination. During curvature domination, the radius of the forward lightcone is

$$\chi_{\text{forward}}(t) = 3 + \ln \frac{t}{t_c} \quad (5.14)$$

while that of the backward lightcone is given by  $\chi_{\text{patch}}$ . Setting the two equal, we find that

$$t_{\text{edge}} = e^{-1} \sqrt{t_c t_\Lambda} . \quad (5.15)$$

One can easily see that  $t_c < t_{\text{edge}} < t_\Lambda$  when  $t_\Lambda \gg t_c$ , which is the limit we are most interested in. So we have, by Eq. (2.3),

$$\chi_{\text{dia}}(t) \propto \begin{cases} 3(t/t_c)^{1/3} & \text{if } t < t_c , \\ 3 + \ln \frac{t}{t_c} & \text{if } t_c \leq t < t_{\text{edge}} , \\ 1 + \ln \frac{t_\Lambda}{t} & \text{if } t_{\text{edge}} \leq t < t_\Lambda , \\ \exp(-t/t_\Lambda + 1) & \text{if } t_\Lambda \leq t . \end{cases} \quad (5.16)$$

When computing the comoving volume, we must keep in mind that space is curved; the comoving volume scales like  $\pi \sinh(2\chi) - 2\pi\chi$ . For large  $\chi$ , this reduces to  $\pi \exp(2\chi)/2$ , while for small  $\chi$  we recover  $4\pi\chi^3/3$ . As an approximation, we will use the exponential form during the period of curvature domination for both the patch and the diamond, as well as during matter domination for the patch. We will use the flat form during matter domination for the diamond, and during  $\Lambda$  domination for both the patch and the diamond. This is a good approximation in the regime where the scales are widely separated. We find

$$V_c^{\text{patch}}(t) \propto \begin{cases} \frac{\pi}{2} \left(\frac{t_\Lambda}{t_c}\right)^2 \exp(8 - 6(t/t_c)^{1/3}) & \text{if } t \ll t_c , \\ \frac{\pi e^2}{2} \left(\frac{t_\Lambda}{t}\right)^2 & \text{if } t_c \ll t \ll t_\Lambda , \\ \frac{4\pi}{3} \exp(-3t/t_\Lambda + 3) & \text{if } t_\Lambda \ll t . \end{cases} \quad (5.17)$$

for the patch and

$$V_c^{\text{dia}}(t) \propto \begin{cases} 36\pi(t/t_c) & \text{if } t \ll t_c , \\ \frac{\pi e^6}{2} \left(\frac{t}{t_c}\right)^2 & \text{if } t_c \ll t < t_{\text{edge}} , \\ \frac{\pi e^2}{2} \left(\frac{t_\Lambda}{t}\right)^2 & \text{if } t_{\text{edge}} \leq t \ll t_\Lambda , \\ \frac{4\pi}{3} \exp(-3t/t_\Lambda + 3) & \text{if } t_\Lambda \ll t . \end{cases} \quad (5.18)$$

for the diamond.

We can count observers in the causal patch or diamond by integrating the comoving volume against  $\dot{n}_{\text{obs}}(t)$ , the rate at which observations are made per unit time and comoving volume. Note that the scale factor in Eq. (5.12) contains an explicit dependence on  $t_c$  during matter domination. This means that the comoving observer density also depends on  $t_c$  through a trivial overall multiplicative factor. But the physical observer density is independent of  $t_c$  during matter domination. It will be clearer to work with a variable that makes this explicit:

$$\dot{\tilde{n}}_{\text{obs}} \equiv \dot{n}_{\text{obs}}(t)/t_c . \quad (5.19)$$

For sufficiently large  $\Delta N$  at fixed  $\Lambda$ , curvature never plays a dynamical role, because  $t_\Lambda < t_c$ . In this regime the number of observers is independent of  $\Delta N$ , and the probability distribution over  $\Delta N$  is given by the prior:

$$\frac{dp}{d\Delta N} \propto \frac{1}{(60 + \Delta N)^4} . \quad (5.20)$$

This can be seen in the 3rd plot of Figs. 2, 5, 8, 11, 14, and 17. In all figures, we have used this analytic formula to continue our results beyond the displayed upper limit of  $\Delta N = 1$  when we calculate probabilities and confidence intervals. The (prior) suppression of large  $\Delta N$  means that there is no runaway in that direction.

Let us turn to the more interesting case where  $t_\Lambda > t_c$ . (In general, there would be two subcases,  $t_\Lambda > t_{\text{peak}} > t_c$  and  $t_\Lambda > t_c > t_{\text{peak}}$ . However, in this subsection we are discussing only the variation of curvature, in a universe otherwise like ours. For all our observer models,  $t_{\text{peak}}$  is comparable to  $t_\Lambda$  in our universe, so the second subcase does not arise.) For the *causal diamond*, we find

$$\frac{dp}{d\Delta N} \propto \frac{1}{(60 + \Delta N)^4} \int_{t_c}^{t_\Lambda} dt \dot{n}_{\text{obs}}(t) \frac{t^2}{t_c} . \quad (5.21)$$

The geometric factor of  $t_c^{-1} \propto \exp(-3\Delta N)$ , along with the prior distribution, favors curvature.

However, for sufficiently large curvature, dynamical effects become important and cut off the probability distribution. With all observer models we consider, the number of observations will decrease if structure formation is suppressed. This effect becomes severe if not even the earliest structures can form, i.e., if the density contrast,  $\sigma(M, t)$ , never reaches unity even for the smallest mass scales that can cool efficiently,  $M_{\text{min}}$ . Let  $t_{\text{vir}}$  denote the time when these structures would have formed in a universe without curvature. By Eq. (3.7), for  $t_c \ll t_{\text{vir}}$  these structures will be suppressed like

$$\exp \left[ - \left( \frac{1.68}{\sqrt{2}\sigma(M, t)} \right)^2 \right] = \exp \left[ -B \left( \frac{t_{\text{vir}}}{t_c} \right)^{4/3} \right] . \quad (5.22)$$

(Here  $B$  is some order-one coefficient and  $t_{\text{vir}}$  depends weakly on the mass scale.) This corresponds to a doubly-exponential suppression of the probability distribution over  $\Delta N$ , Eq. (5.21). In our universe, the value of  $t_c$  corresponding to  $\Delta N = 0$  is somewhat larger than  $t_{\text{vir}}$ , and the suppressed regime is reached close to the lower end of our parameter space,  $\Delta N = -3.5$ . This can be seen in the 3rd plot of Figs. 2, 5, and 8.

Now let us consider the same regime,  $t_\Lambda > t_c$ , in the *causal patch*. Using Eq. (5.17) we find

$$\frac{dp}{d\Delta N} \propto \frac{\pi e^2/2}{(60 + \Delta N)^4} \int_{t_c}^{t_\Lambda} dt \dot{n}_{\text{obs}}(t) \frac{t_c t_\Lambda^2}{t^2} . \quad (5.23)$$

This time, a geometric factor of  $t_c$  appears in the numerator, suppressing curvature. Below  $\Delta N \approx -3.5$ , the stronger, dynamical suppression discussed for the diamond sets in: the failure of structure formation. This behavior is reflected in the 3rd plot of Figs. 11, 14, and 17.

In all plots and all observer models, our failure thus far to detect curvature is not surprising; it is perfectly compatible with the predicted probability distribution. However, upcoming experiments such as Planck will be more sensitive to small amounts of spatial curvature. In the spirit of Ref. [40], let us use our probability distribution to calculate the probability that curvature will be detected in the future.

The current  $1\sigma$  bound on curvature from WMAP5+BAO+SN [50] is  $\Omega_k = -0.0050_{-0.0060}^{+0.0061}$ . This corresponds roughly to the Gaussian distribution

$$\frac{dp_{\text{exp}}}{d\Omega_k} \propto \exp\left(-\frac{(\Omega_k + .0050)^2}{2(.0061)^2}\right). \quad (5.24)$$

Our convention for  $\Delta N = 0$  is the upper  $1\sigma$  bound,  $\Omega_k = .0011$ . Since  $\Omega_k \propto \exp(-2\Delta N)$ , we can convert our probability distribution for  $\Delta N$  into one for  $\Omega_k$ , which in the regime  $\Delta N \gtrsim -1$  looks like

$$\frac{dp}{d\Omega_k} \propto \frac{1}{\Omega_k} \frac{1}{\left(60 + \frac{1}{2} \ln \frac{.0011}{\Omega_k}\right)^4}, \quad (5.25)$$

Because we are assuming an open universe, the probability for  $\Omega_k < 0$  vanishes. The current experimental bound is so strong that we do not need a more detailed form. If future experiments reach a sensitivity level of  $\Delta\Omega_k$ , then we will be able to detect the openness of the universe if  $\Omega_k \geq \Delta\Omega_k$ . The probability for this to occur is

$$p(\Omega_k \geq \Delta\Omega_k) = \int_{\Delta\Omega_k}^{\infty} \frac{dp_{\text{expt}}}{d\Omega_k}(\Omega_k) \frac{dp}{d\Omega_k}(\Omega_k) d\Omega_k \quad (5.26)$$

$$\propto \int_{\Delta\Omega_k}^{\infty} \frac{d\Omega_k}{\Omega_k} \frac{\exp\left(-\frac{(\Omega_k + .0050)^2}{2(.0061)^2}\right)}{\left(60 + \frac{1}{2} \ln \frac{.0011}{\Omega_k}\right)^4}, \quad (5.27)$$

which is normalized so that  $p(\Omega_k \geq 0) = 1$ . Then we find  $p(\Omega_k \geq 10^{-3}) \approx 0.033$ , which might be realized in the near future, and  $p(\Omega_k \geq 10^{-4}) \approx 0.088$ , which is roughly the limit of achievable sensitivity.

### 5.3 Varying both the cosmological constant and curvature

When both the curvature and the cosmological constant vary, we can use a similar analysis to obtain a qualitative understanding of the probability distributions. Again,

we will distinguish different regimes determined by the relative sizes of  $t_\Lambda$ ,  $t_c$ , and  $t_{\text{peak}}$ . We will now have to consider both positive and negative values of the cosmological constant.

The cases with  $t_\Lambda \ll t_c$  correspond to negligible curvature. In this regime, the joint probability distribution is the direct product of the probability distribution over  $\Lambda$  (with negligible curvature, see Sec. 5.1) and the prior probability distribution over  $\Delta N$  (see Eq. (2.7). which we have already examined. We can also immediately dispense with the cases  $t_\Lambda \ll t_{\text{peak}}$ : there will always be pressure toward smaller  $|\Lambda|$  either because of suppressed structure formation and a small causal diamond/patch ( $\Lambda > 0$ ) or because the universe has already collapsed ( $\Lambda < 0$ ).

The case  $t_c \ll t_{\text{peak}} \ll t_\Lambda$ , for  $\Lambda > 0$ , was essentially discussed in the previous subsection, except that  $\Lambda$  was held fixed there. But since  $t_{\text{peak}}$  is essentially independent of  $\Lambda$  and  $\Delta N$ ,  $\Lambda$  can vary only in the direction of smaller values while preserving the above inequality. Therefore, in this regime, the joint probability distribution is the direct product of the probability distribution over  $\Lambda$  given in Sec. 5.1 and the distribution over  $\Delta N$  derived in Sec. 5.2. Moreover, the doubly-exponential suppression of structure formation by curvature is unaffected by the sign of  $\Lambda$ . Therefore, the joint distribution over  $\Delta N$  and negative values of  $\Lambda$  is given by the direct product of the  $\Delta N$  distribution from Sec. 5.2 and the negative  $\Lambda$  distribution from Sec. 5.1.

There is one subtlety, which is apparent when comparing the 3rd plot of Fig. 2 with that of Fig. 3. In Fig. 3 the probability is *increasing* toward the boundary of the plot at  $\Delta N = -3.5$ , whereas in Fig. 2 the suppression of structure formation has caused the probability distribution to *decrease* at the same value of  $\Delta N$ . We have already argued above that structure suppression due to large curvature works the same way for  $\Lambda < 0$  as for  $\Lambda > 0$ , so we must reconcile the apparent discrepancy. First, we should note that the probability does not increase indefinitely in toward small  $\Delta N$ , our plot range is merely inadequate to show the eventual peak and subsequent decrease. We must explain why the suppression does not happen at the same value of  $\Delta N$  in the positive and negative cases, for equal values of  $|\Lambda|$ .

The answer lies in the geometry of the causal diamond, specifically in the difference in edge times,  $t_{\text{edge}}$ , for positive and negative  $\Lambda$ . As we saw in Eq. (5.15),  $t_{\text{edge}}$  will actually decrease as curvature is increased while  $\Lambda$  remains constant. It turns out that  $t_{\text{edge}} \approx t_{\text{peak}}$  for  $\Lambda = \Lambda_0$ ,  $Q = Q_0$ , and  $\Delta N = -3.5$ . However,  $t_{\text{edge}}$  for  $\Lambda < 0$  is always of order  $t_\Lambda$  (to be precise, it is equal to the time of maximum expansion). In particular,  $t_{\text{edge}} \gg t_{\text{peak}}$  for  $Q = Q_0$ ,  $\Lambda = -\Lambda_0$  and all values of  $\Delta N$ . The entropy production curves are nearly identical when the sign of  $\Lambda$  is flipped (since we are safely in the limit  $t_\Lambda \gg t_{\text{peak}}$ ), but in the  $\Lambda < 0$  case the tail of the entropy production lies entirely within the growing phase of the causal diamond. The extra boost in probability granted by

this effect means that more curvature is required to suppress the *probability* for  $\Lambda < 0$ , even though *structure formation* is suppressed by an amount independent of the sign of  $\Lambda$ .

Let us turn to the case

$$t_{\text{peak}} \ll t_c \ll t_\Lambda; \quad \Lambda > 0 . \quad (5.28)$$

Structure formation is uninhibited in this regime, so only prior probabilities and geometric effects control the joint probability distribution. The comoving volumes of the patch and diamond are given in Eqs. 5.17 and 5.18. Combining this with the prior distribution, we find for the *causal diamond*:

$$\frac{d^2 p}{d \log_{10} \Lambda d \Delta N} \propto \frac{\Lambda}{(60 + \Delta N)^4} \int_0^{t_c} dt \dot{n}(t) t . \quad (5.29)$$

The integral is independent of  $\Lambda$  and  $\Delta N$ , so the probability distribution is governed by the prefactor. The pressure is toward larger  $\Lambda$  and smaller  $\Delta N$  suppresses any hierarchy between the timescales appearing in the above double inequality. Indeed, in our universe, the inequality is either violated or approximately saturated.

In the same regime, Eq. (5.28), the *causal patch* introduces the geometric factor  $t_\Lambda^2/t_c$ . This leads to a somewhat different result:

$$\frac{d^2 p}{d \log_{10} \Lambda d \Delta N} \propto \frac{\Lambda}{(60 + \Delta N)^4} \int_0^{t_c} dt \dot{n}(t) \frac{t_\Lambda^2}{t_c} \exp(8 - 6(t/t_c)^{1/3}) \quad (5.30)$$

$$\propto \frac{1}{(60 + \Delta N)^4} \exp(-3\Delta N) . \quad (5.31)$$

There is a pressure toward smaller  $\Delta N$ , suppressing a large hierarchy  $t_{\text{peak}} \ll t_c$ . This is qualitatively the same as for the diamond, though the pressure is stronger. But unlike in the diamond case, small values of the cosmological constant are unsuppressed: at fixed  $\Delta N$ , the probability is flat in  $\log_{10} \Lambda$ . This is a runaway problem: Without a lower bound on  $\log_{10} \Lambda$ , the probability distribution is not integrable in the direction of small  $\log_{10} \Lambda$ . Such a lower bound may well be supplied by the finiteness of the landscape. It need not be particularly close to the observed value, since the probability is flat. (We are about to discover, however, that a more severe runaway problem arises for the causal patch in the analogous case with negative  $\Lambda$ .)

Now we analyze the same case, Eq. (5.28), but with  $\Lambda < 0$ . Our conclusions for the *causal diamond* remain the same, with  $\Lambda$  replaced by  $|\Lambda|$ , since neither  $\dot{n}_{\text{obs}}(t)$  nor  $V_c^{\text{dia}}(t)$  depend on the sign of  $\Lambda$  when  $t \ll t_c \ll t_\Lambda$ . Turning to the *causal patch*, we

note that the scale factor can be approximated by

$$a(t) = \begin{cases} t^{2/3} t_c^{1/3} & \text{if } t < t_c , \\ t_\Lambda \sin\left(\frac{t+t_1}{t_\Lambda}\right) & \text{if } t_c \leq t < t_2 - t_c , \\ (t_2 - t)^{2/3} t_c^{1/3} & \text{if } t_2 - t_c \leq t < t_2 . \end{cases} \quad (5.32)$$

in the simplified sudden transition approximation, where

$$t_1 = t_\Lambda \sin^{-1}\left(\frac{t_c}{t_\Lambda}\right) - t_c \quad (5.33)$$

and

$$t_2 = \pi t_\Lambda - 2t_1 . \quad (5.34)$$

Since  $t_{\text{peak}} \ll t_c$ , we need only compute the comoving volume in the regime  $t \ll t_c$ . For the comoving radius, we find

$$\chi_{\text{patch}}(t) = \int_t^{t_2} \frac{dt}{a(t)} \quad (5.35)$$

$$= \int_t^{t_c} \frac{1}{t^{2/3} t_c^{1/3}} + \int_{t_c}^{t_2-t_c} \frac{dt}{t_\Lambda \sin\left(\frac{t+t_1}{t_\Lambda}\right)} + \int_{t_2-t_c}^{t_2} \frac{1}{(t_2-t)^{2/3} t_c^{1/3}} \quad (5.36)$$

$$= 6 - 3 \left(\frac{t}{t_c}\right)^{1/3} + \ln \frac{\tan(t_2/2t_\Lambda - t_c/2t_\Lambda + t_1/2t_\Lambda)}{\tan(t_c/2t_\Lambda + t_1/2t_\Lambda)} \quad (5.37)$$

$$\approx 6 + 2 \ln \frac{2t_\Lambda}{t_c} . \quad (5.38)$$

(In the final line we used  $t \ll t_c \ll t_\Lambda$ .) Using  $V(\chi) \propto \exp(2\chi)$ , the comoving volume is approximately

$$V_c^{\text{patch}}(t) \propto \left(\frac{t_\Lambda}{t_c}\right)^4 , \quad (5.39)$$

yielding the probability distribution

$$\frac{d^2 p}{d \log_{10} |\Lambda| d \Delta N} \propto \frac{\exp(-9\Delta N)}{|\Lambda| (60 + \Delta N)^4} . \quad (5.40)$$

Again we find the causal patch leads to runaway towards small values of  $|\Lambda|$  in the presence of curvature. The runaway is stronger, like  $|\Lambda|^{-1}$  for fixed  $\Delta N$ , than the flat distribution over  $\log_{10} |\Lambda|$  that we found in the case of positive  $\Lambda$ . The preference for small  $|\Lambda|$  is evident in the 8th plot of Figs. 12, 15, and 18, where the probability is concentrated in the small  $\Delta N$  and small  $\Lambda$  corner of the plots.

This runaway implies one of two things. Either the causal patch is the wrong measure, at least in regions with nonpositive cosmological constant.<sup>9</sup> Or our vacuum has the smallest cosmological constant of all (anthropic) vacua in the landscape. The latter possibility is quite interesting, since it offers a potential first-principles explanation of the actual magnitude of  $|\Lambda|$  (and by correlation, many other unexplained hierarchies) in terms of a fundamental property of the underlying theory: the size of the landscape. (A variant of this possibility is that the landscape does contain vacua with smaller  $\Lambda$  but the prior probability distribution for  $\Delta N$  is weighted towards large values, so that curvature is negligible in all pocket universes.)

#### 5.4 Varying the density contrast only

Unlike  $\Lambda$  and  $\Delta N$ ,  $Q$  has no geometric effects (at least in the homogeneous approximation we employ). It does have dynamical implications, however. The effects of  $Q$  on the observer production rate  $\dot{n}_{\text{obs}}$  differ somewhat depending on the observer model. Since all three models involve star formation, let us begin by considering how it is affected by  $Q$ .  $Q$  enters the structure formation equations in the combination  $QG(t)$ , and  $G(t) \propto t^{2/3}$  during matter domination. Thus, the time of structure formation (and thus, star formation) scales as  $t_{\text{vir}} \sim Q^{-3/2}$ .

Let us discuss first the effects of increasing  $Q$ . Star formation that happens earlier also happens faster. The star formation rate for a single halo, Eq. (3.8), scales like the inverse of the gravitational timescale of the halo. Since  $t_{\text{grav}}$  is proportional to the virialization time of the halo, the star formation rate scales as  $\dot{\rho}_*(t_{\text{peak}}) \propto Q^{3/2}$ . By similar arguments, the width of the star formation rate also scales like  $\Delta t \propto Q^{-3/2}$ . Thus, one might expect that the total integrated star formation rate stays constant as one varies  $Q$ . However, there is an effect which is not seen by this rough analysis. As  $Q$  increases, the range of halo masses which are able to cool and form stars also increases. The lower mass limit, which comes from the requirement that halos be hotter than  $10^4 K$  to start, is smaller at earlier times. And the upper mass barrier, which arises from radiative cooling failure, completely disappears at sufficiently early times (prior to about 1 Gyr), because Compton cooling becomes efficient [51].<sup>10</sup> Thus, a larger mass fraction forms stars. Numerically, we find that these two effects combine to make the

---

<sup>9</sup>These regions were defined more sharply in Ref. [19,21] (“hat domains” and “singular domains”). If the causal patch is viewed as arising from an analogy with the AdS/CFT correspondence via a global/local duality, it is not implausible that it may apply only in the “eternal domain” (roughly, regions with positive  $\Lambda$ ).

<sup>10</sup>Dominant Compton cooling, however, corresponds to a drastic change of regime and may be catastrophic. This possibility is explored in Ref. [25].

integrated star formation grow roughly logarithmically with  $Q$ :

$$\int dt \dot{\rho}_*(t) \propto \log_{10} Q . \quad (5.41)$$

In the entire analysis, so far, we have assumed that structure formation is not disrupted by curvature or vacuum energy; this assumption is certainly justified in the case at hand, where  $\Lambda$  and  $\Delta N$  are held fixed and set to the observed values.

There is a limit to how far we can increase  $Q$  given the model of star formation outlined in Sec. 3.1: for large enough  $Q$ , structure formation happens before recombination. Even though dark matter halos can form prior to recombination, baryons cannot collapse into galaxies. One expects that if there are large dark matter halos already formed at the time of recombination, then there will be a huge surge in star formation as the baryons fall into them after decoupling from the photons. Our star formation code takes this into account in a very simplistic way: star formation which would have happened prior to recombination is delayed until after recombination, and at that time there is a large and essentially instantaneous spike in the star formation rate, after which it drops back down to normal levels. (The code knows nothing of the actual interactions between baryons and photons.) There may be a phenomenological reason why such instantaneous star formation is not hospitable for observers, but at the very least this is a change in regime for the star formation rate. At  $Q = 10^2 Q_0$ , 32% of the total star formation is created in this spike, up from 13% at  $10^{1.75} Q_0$  and 0.1% at  $10^{1.5} Q_0$ , and this percentage will continue to rise if  $Q$  is increased. This motivates our cut-off at  $10^2 Q_0$ . As seen in Sec. 4, the behavior of the probability distribution in  $Q$  near the upper boundary is fairly mild (at worst a logarithmic growth when  $\Lambda = \Lambda_0$  and  $\Delta N > 0$  are fixed), so our results should not change dramatically if the cut-off is extended.

If  $Q$  is decreased compared to the observed value, then the range of halo masses that can cool efficiently shrinks. It soon disappears altogether, for  $Q \approx 10^{-1} Q_0$ . There are no stars, and no observers, for smaller values of  $Q$ . This cuts off the probability distribution over  $Q$  independently of  $\Delta N$ ,  $\Lambda$ , the measure, and the observer model, so we will not discuss this case further.

Let us now estimate the probability distribution for  $Q > Q_0$ . We begin with the time delay observer models. The time delay is held fixed as  $Q$  varies. (The assumption underlying these models is that  $t_{\text{delay}}$  is determined, at least in a substantial part, by dynamics unrelated to  $Q$ ,  $\Delta N$ , or  $\Lambda$ ). In our universe,  $t_{\text{vir}}$  is already somewhat smaller than 5 Gyr, and for larger  $Q$ ,  $t_{\text{vir}}$  will be entirely negligible compared to the time delay, as will the width of the star formation rate. Thus, observers will live at a time given approximately by  $t_{\text{delay}}$ . Using a flat prior,  $d\tilde{p}/d \log_{10} Q \sim 1$ , and the logarithmic

growth of the integrated SFR described, one expects

$$\frac{dp}{d\log_{10} Q} \propto \int dt \dot{\rho}_*(t - t_{\text{delay}}) V_c(t_{\text{delay}}) \quad (5.42)$$

$$\propto \log_{10} Q . \quad (5.43)$$

This distribution holds in both the patch and the diamond and with either a 5 or 10 Gyr time delay, as is evident in the 2nd plot of Figs. 5, 8, 14, and 17.

There are additional complications with entropy production, and these complications are such that we are only able to give a very rough qualitative account of the probability distribution; numerical calculations are essential to finding the true shape. The first complication is that stars burn for a long time after they are created. This makes the entropy production rate significantly broader than the star formation rate, and the result is that we cannot reliably approximate all of the entropy as being created at a single time.

A second complication is that earlier star formation means earlier entropy production, because much of the entropy is produced by fast burning massive stars. The peak of the entropy production rate can happen at arbitrarily early times, unlike in the time delay models, which ensured that the peak of  $\dot{n}_{\text{obs}}(t)$  happens after the time  $t_{\text{delay}}$ . This has an important consequence in the comparison of the patch and the diamond. As  $Q$  is increased, more entropy production happens at earlier times, when the diamond is small but the patch is large. Indeed, comparing the 2nd plot of Figs. 2 and 11, we see that for the *causal diamond*,  $dp/d\log_{10} Q$  is maximal at  $Q = Q_0$ ; whereas for the *causal patch*, it increases monotonically with  $\log_{10} Q$ .

The third complication is the effect of the dust temperature. The interstellar dust temperature is a complicated function of both the halo virialization time and the actual emission time (Eq 3.16). However, we can say qualitatively that the effect of variation in dust temperature is to suppress the entropy production of early-time stars relative to late-time stars. This is why, for example, in the 2nd plot of Fig. 11, which uses the causal patch measure, the probability distribution begins to flatten out for large  $Q$  rather than continuing to increase in a manner similar to that of the time delay model in Figs. 5 and 8.

## 5.5 Varying the density contrast and the cosmological constant

When both  $\Lambda$  and  $Q$  are allowed to vary, we can combine the analysis of Sec. 5.1 and the previous subsection to understand the probability distribution. In Sec. 5.1, we concluded that the most likely value of  $\Lambda$  for fixed  $Q$  was determined by the condition  $t_\Lambda \approx t_{\text{peak}}$ , where  $t_{\text{peak}}$  is the peak time of the model-dependent  $\dot{n}_{\text{obs}}(t)$ . In the previous subsection we found that depending on the observer model,  $t_{\text{peak}}$  can depend on  $Q$ .

In the time delay observer model,  $t_{\text{peak}} \approx t_{\text{delay}}$  for all relevant values of  $Q$ . Indeed, in the 9th plots of Figs. 5, 8, 14, and 17, we see that the most likely value of  $\Lambda$  is essentially independent of  $Q$ . Additionally, the probability increases with  $Q$  proportional to  $\log_{10} Q$ , due to the increase of total star formation discussed in Sec. 5.4, and this effect is visible in the same plots. The only difference between the diamond and the patch in these models is in the broadness of the distribution in the  $\Lambda$  direction, which was also discussed in Sec. 5.1.

In the entropy production observer model,  $t_{\text{peak}}$  depends strongly on  $Q$ :  $t_{\text{peak}} \propto Q^{-3/2}$ . This leads to the relation  $\Lambda \propto Q^3$  for the most likely value of  $\Lambda$  at a given  $Q$ . In this 9th plot of Figs. 2, 3, 11, and 12 we see this trend in the slope of the contour lines toward large  $\Lambda$  and large  $Q$ . This looks like a runaway, but there is a cut-off ( $Q \sim 10^2 Q_0$ ) coming from our requirement that star formation happen after recombination (see Sec. 5.4).

## 5.6 Varying the density contrast and spatial curvature

If curvature is small,  $t_c \gg t_{\text{vir}}$ , curvature has neither dynamical nor geometric effects for  $\Lambda = \Lambda_0$ . Large curvature, however, can disrupt structure formation and thus star formation. This is encoded in Eq. (5.22), which is valid for  $t_c \ll t_{\text{vir}}$  (and was derived from Eq. (3.7)). When  $Q$  varies simultaneously with  $\Delta N$ , we must take into account the  $Q$ -dependence of  $t_{\text{vir}}$ ,  $t_{\text{vir}} \sim Q^{-3/2}$ :

$$\exp \left[ -B \left( \frac{t_{\text{vir}}}{t_c} \right)^{4/3} \right] = \exp \left[ -C Q^{-2} \left( \frac{t_{\text{eq}}}{t_c} \right)^{4/3} \right]. \quad (5.44)$$

(Recall that  $B$  is an order-one coefficient;  $C$  is a different order-one coefficient that weakly depends on the mass scale.) For increased  $Q$  a smaller  $t_c$  is required to halt structure formation. This yields the following relation between  $\log_{10} Q$  and  $\Delta N_{\text{crit}}$ , the value of  $\Delta N$  at which structure formation is completely suppressed:

$$(2 \log_{10} e) \Delta N_{\text{crit}} + \log_{10} Q = \text{const.} \quad (5.45)$$

We found in Sec. 5.2 that  $\Delta N_{\text{crit}} \approx -3.5$  when  $Q = Q_0$ , which is already at the edge of the parameter range we consider. For larger values of  $Q$  the value of  $\Delta N$  necessary to significantly suppress structure formation is outside that range. However, the highest value of  $Q$  we consider,  $10^2 Q_0$ , shifts  $\Delta N_{\text{crit}}$  only by -2.3.

The 7th plot of each figure shows how  $\Delta N_{\text{crit}}$  depends on  $Q$  for fixed  $\Lambda = \Lambda_0$ . In the time delay models, Figs. 5, 8, 14, and 17, one clearly sees the contours of constant probability following a slope given approximately by Eq. (5.45). The corresponding plots in the entropy production models, Figs 2 and 11, look a bit different in their gross

features, owing to the complications discussed in Sec. 5.4, but the same trend in  $\Delta N_{\text{crit}}$  is visible.

All of the above considerations hold also for  $\Lambda = -\Lambda_0$  for the *causal diamond*, which can be seen in the 7th plot of Figs. 3, 6, and 9. (The *causal patch*, of course, has a runaway problem which is dominant. See Sec. 5.3.) Since  $t_{\text{rmedge}}$  is larger for  $\Lambda < 0$  for equal  $|\Lambda|$  (see Sec. 5.1), the geometry of the diamond allows  $\Lambda < 0$  to tolerate more curvature. This means  $\Delta N_{\text{crit}}$  is smaller for  $\Lambda < 0$ , but does not change the fact that it scales according to Eq. (5.45). It is this geometric effect which also leads to the enhancement of probability for small  $\Delta N$  visible in the 3rd and 6th plots of those same figures. As our discussion has made clear, this does not indicate a new runaway problem; our displayed parameter range is merely too small to see the suppression at small  $\Delta N$  from structure suppression.

## 5.7 Marginalizing

Let us combine our previous observations to understand the behavior of the probability distributions in which one or more parameters have been integrated out.

**Integrating out  $\Delta N$**  For the *causal diamond*, the only consequence of varying  $\Delta N$  is that for small  $\Delta N$  structure formation is interrupted. This only happens over a very small part of the full  $\Delta N$  parameter space, so integrating out  $\Delta N$  does not have a large effect on the distributions for  $Q$  and  $\Lambda$ , independently of the observer model. This is evident in the similarities between the 9th and 12th plots in Figs. 2, 3, 5, 6, 8, and 9.

For the *causal patch*, however, the runaway toward small  $|\Lambda|$  discussed in Sec. 5.3 means that the smallest values of  $|\Lambda|$  are greatly favored after  $\Delta N$  is integrated out. Restricting to  $\Lambda > 0$ , the effect is weaker, but can still be seen in the comparison of the 9th and 12th plots of Figs. 14 and 17. For  $\Lambda < 0$ , it is stronger, as seen in comparing the 9th and 12th plots in Figs. 12, 15, and 18.

**Integrating out  $Q$**  The effect of integrating out  $Q$  depends on the observer model. In the time delay models, there is very little change in the distributions of  $\Lambda$  or  $\Delta N$  after integrating out  $Q$ , as one can see by comparing the 8th and 11th plots in each of Figs. 5, 6, 8, and 9. For  $\Lambda$ , this is easily understood since most of the  $Q$  parameter space has  $t_{\text{peak}} = t_{\text{delay}}$ , and thus the analysis is largely independent of  $Q$  (see Sec. 5.4). For curvature, integrating out  $Q$  should increase the relative probability for small  $\Delta N$  compared with  $Q = Q_0$  due to relaxed restrictions on structure formation. Comparing the 3rd and 6th plots of those same figures, we see that small  $\Delta N$  is relatively more favored in the 6th plot.

For entropy production, though, there are some more significant effects. After integrating out  $Q$ , larger values of both  $|\Lambda|$  and curvature are generally favored. There

are two reasons for this. The first is that the prior probabilities for  $|\Lambda|$  and curvature want both of them to be large. With  $Q$  fixed, this tendency for largeness is countered by the suppression of structure formation when  $\Lambda$  or curvature dominate before  $t_{\text{peak}}$ . But once  $Q$  is integrated out, this restriction is relaxed. The second reason is that the large  $Q$  region of parameter space, which is where  $\Lambda$  and curvature are allowed to be large, has more star formation and hence more entropy per comoving volume. So the large  $Q$  region of parameter space contributes more to the resulting distributions of  $\Lambda$  and  $\Delta N$  than the small  $Q$  region after  $Q$  is integrated out.

It is difficult to find an analytical formula for the resulting probability distributions due to the complications mentioned in Sec. 5.4. But, qualitatively, we can see this shift toward larger  $|\Lambda|$  and smaller  $\Delta N$  in comparing the 8th and 11th plots in each of Figs. 2, 3, and 11 (Fig. 12 is not included on this list because the runaway problem toward small  $|\Lambda|$  is the dominant feature for  $\Lambda < 0$  in the causal patch). The same figures also show a preference for large  $|\Lambda|$  in the 4th plot. The probability flattens or turns around for the largest values of  $|\Lambda|$  because of the upper limit we have imposed on  $Q$ .

**Integrating out  $\Lambda$**  When integrating out  $\Lambda$ , the most important distinction is whether we use the diamond or the patch. For the *causal patch*, as discussed in Sec. 5.3, there is a runaway problem toward small  $\Lambda$ . The probability is concentrated in the region of smallest  $|\Lambda|$ . It is possible that this value is not much smaller than the observed value, so this problem is not necessarily fatal. When computing confidence intervals requires the assumption of a lower bound on  $|\Lambda|$  (which is always highlighted in the captions), we use the lower end of the displayed range,  $10^{-3}\Lambda_0$ .

This issue does not arise for the *causal diamond*. In the time delay models there is almost no difference between leaving  $\Lambda$  fixed and integrating it out in both the positive and negative cases. We can see this by comparing the 7th and 10th plots of Figs. 5, 6, 8, and 9. The cases where  $\Lambda$  is integrated over both positive and negative values are covered in Figs. 7 and 10. They are almost identical to the negative  $\Lambda$  case because the  $\Lambda < 0$  vacua contribute the bulk of the probability.

With entropy production there is a qualitative change in the distribution of  $Q$  when going from  $\Lambda$  fixed to  $\Lambda$  integrated out. This change is most clearly seen in comparing the 2nd and 5th plots of Figs. 2 and 3. When  $\Lambda$  is fixed, the  $Q$  distribution becomes flat for large  $Q$ , and also has a peak at small  $Q$  ( $\approx Q_0$ ). Recall from Sec. 5.4 that the flatness for large  $Q$  is attributable to the changing dust temperature, and the shape of the diamond gives extra suppression for large  $Q$  that effectively creates the peak at small  $Q$ . After integrating out  $\Lambda$ , both of these effects disappear. (In the plots referenced above, it looks like large  $Q$  is actually still suppressed, but this is due to a

new effect: the finiteness of our parameter range in  $\Lambda$ ).

The reason why these effects disappear is because at fixed  $\Lambda$  and high  $Q$  the diamond is sensitive to the long tail of the entropy production rate; its maximal comoving volume is several Gyr after  $t_{\text{peak}}$ . Integrating over  $\Lambda$  is effectively like finding the optimal value of  $\Lambda$  for each  $Q$ . The optimal value for  $\Lambda$  is the one where the maximal height diamond volume is centered on the peak of the entropy production rate, which means resulting  $Q$  distribution is insensitive to the tail of the entropy production rate.

## Acknowledgments

We are grateful to B. Freivogel, R. Harnik, and J. Niemeyer for discussions. This work was supported by the Berkeley Center for Theoretical Physics, by a CAREER grant (award number 0349351) of the National Science Foundation, by fqxi grant RFP2-08-06, and by the US Department of Energy under Contract DE-AC02-05CH11231.

## References

- [1] R. Bousso and J. Polchinski, “Quantization of four-form fluxes and dynamical neutralization of the cosmological constant,” *JHEP* **06** (2000) 006, [hep-th/0004134](#).
- [2] S. Kachru, R. Kallosh, A. Linde, and S. P. Trivedi, “De Sitter vacua in string theory,” *Phys. Rev. D* **68** (2003) 046005, [hep-th/0301240](#).
- [3] A. N. Schellekens, “The landscape ‘avant la lettre’,” [arXiv:physics/0604134](#).
- [4] S. Weinberg, “Anthropic bound on the cosmological constant,” *Phys. Rev. Lett.* **59** (1987) 2607.
- [5] J. Polchinski, “The cosmological constant and the string landscape,” [hep-th/0603249](#).
- [6] R. Bousso, “TASI Lectures on the Cosmological Constant,” *Gen. Rel. Grav.* **40** (2008) 607–637, [arXiv:0708.4231 \[hep-th\]](#).
- [7] R. Bousso and S. Leichenauer, “Star formation in the multiverse,” *Phys. Rev.* **D79** (2009) 063506, [arXiv:0810.3044 \[astro-ph\]](#).
- [8] A. Linde, D. Linde, and A. Mezhlumian, “Nonperturbative amplifications of inhomogeneities in a self-reproducing universe,” *Phys. Rev. D* **54** (1996) 2504–2518, [gr-qc/9601005](#).
- [9] A. H. Guth, “Inflation and eternal inflation,” *Phys. Rep.* **333** (1983) 555, [astro-ph/0002156](#).

- [10] A. H. Guth, “Inflationary models and connections to particle physics,” [astro-ph/0002188](#).
- [11] A. H. Guth, “Inflation,” [astro-ph/0404546](#).
- [12] M. Tegmark, “What does inflation really predict?,” *JCAP* **0504** (2005) 001, [astro-ph/0410281](#).
- [13] R. Bousso, B. Freivogel, and I.-S. Yang, “Boltzmann babies in the proper time measure,” *Phys. Rev.* **D77** (2008) 103514, [arXiv:0712.3324 \[hep-th\]](#).
- [14] R. Bousso and B. Freivogel, “A paradox in the global description of the multiverse,” *JHEP* **06** (2007) 018, [hep-th/0610132](#).
- [15] D. N. Page, “Is our universe likely to decay within 20 billion years?,” [hep-th/0610079](#).
- [16] D. N. Page, “Return of the Boltzmann brains,” [hep-th/0611158](#).
- [17] A. Linde, “Towards a gauge invariant volume-weighted probability measure for eternal inflation,” *JCAP* **0706** (2007) 017, [arXiv:0705.1160 \[hep-th\]](#).
- [18] A. H. Guth, “Eternal inflation and its implications,” *J. Phys.* **A40** (2007) 6811–6826, [hep-th/0702178](#).
- [19] R. Bousso, “Complementarity in the Multiverse,” [arXiv:0901.4806 \[hep-th\]](#).
- [20] R. Bousso, B. Freivogel, and I.-S. Yang, “Properties of the scale factor measure,” [arXiv:0808.3770 \[hep-th\]](#).
- [21] R. Bousso and I.-S. Yang, “Global-Local Duality in Eternal Inflation,” [arXiv:0904.2386 \[hep-th\]](#).
- [22] R. Bousso, “Holographic probabilities in eternal inflation,” *Phys. Rev. Lett.* **97** (2006) 191302, [hep-th/0605263](#).
- [23] R. Bousso, R. Harnik, G. D. Kribs, and G. Perez, “Predicting the cosmological constant from the causal entropic principle,” *Phys. Rev. D* **76** (2007) 043513, [hep-th/0702115](#).
- [24] B. Freivogel, “Anthropic Explanation of the Dark Matter Abundance,” [arXiv:0810.0703 \[hep-th\]](#).
- [25] R. Bousso, L. J. Hall, and Y. Nomura, “Multiverse Understanding of Cosmological Coincidences,” [arXiv:0902.2263 \[hep-th\]](#).
- [26] J. Garriga and A. Vilenkin, “Holographic Multiverse,” *JCAP* **0901** (2009) 021, [arXiv:0809.4257 \[hep-th\]](#).

- [27] R. Bousso, B. Freivogel, and M. Lippert, “Probabilities in the landscape: The decay of nearly flat space,” *Phys. Rev.* **D74** (2006) 046008, [hep-th/0603105](#).
- [28] L. Mersini-Houghton and F. C. Adams, “Limitations of anthropic predictions for the cosmological constant  $\Lambda$ : Cosmic Heat Death of Anthropic Observers,” *Class. Quant. Grav.* **25** (2008) 165002, [arXiv:0810.4914](#).
- [29] F. Denef and M. R. Douglas, “Distributions of flux vacua,” *JHEP* **05** (2004) 072, [hep-th/0404116](#).
- [30] J. M. Cline, A. R. Frey, and G. Holder, “Predictions of the causal entropic principle for environmental conditions of the universe,” [arXiv:0709.4443 \[hep-th\]](#).
- [31] B. Bozek, A. J. Albrecht, and D. Phillips, “Curvature Constraints from the Causal Entropic Principle,” [arXiv:0902.1171 \[astro-ph.CO\]](#).
- [32] D. Phillips and A. Albrecht, “Effects of Inhomogeneity on the Causal Entropic prediction of Lambda,” [arXiv:0903.1622 \[gr-qc\]](#).
- [33] L. Hernquist and V. Springel, “An analytical model for the history of cosmic star formation,” *Mon. Not. Roy. Astron. Soc.* **341** (2003) 1253, [arXiv:astro-ph/0209183](#).
- [34] M. P. Salem, “Negative vacuum energy densities and the causal diamond measure,” [arXiv:0902.4485 \[hep-th\]](#).
- [35] L. Susskind, L. Thorlacius, and J. Uglum, “The stretched horizon and black hole complementarity,” *Phys. Rev. D* **48** (1993) 3743, [hep-th/9306069](#).
- [36] R. Bousso, B. Freivogel, and I.-S. Yang, “Eternal inflation: The inside story,” *Phys. Rev. D* **74** (2006) 103516, [hep-th/0606114](#).
- [37] J. B. Hartle and M. Srednicki, “Are we typical?,” *Phys. Rev. D* **75** (2007) 123523, [arXiv:0704.2630 \[hep-th\]](#).
- [38] J. Garriga and A. Vilenkin, “Prediction and explanation in the multiverse,” [arXiv:0711.2559 \[hep-th\]](#).
- [39] D. N. Page, “The Born Rule Dies,” [arXiv:0903.4888 \[hep-th\]](#).
- [40] B. Freivogel, M. Kleban, M. Rodriguez Martinez, and L. Susskind, “Observational consequences of a landscape,” *JHEP* **03** (2006) 039, [arXiv:hep-th/0505232](#).
- [41] D. Schwartz-Perlov and A. Vilenkin, “Probabilities in the Bousso-Polchinski multiverse,” *JCAP* **0606** (2006) 010, [hep-th/0601162](#).
- [42] D. Schwartz-Perlov, “Probabilities in the Arkani-Hamed-Dimopolous-Kachru landscape,” [hep-th/0611237](#).

- [43] K. D. Olum and D. Schwartz-Perlov, “Anthropic prediction in a large toy landscape,” [arXiv:0705.2562 \[hep-th\]](#).
- [44] D. Schwartz-Perlov, “Anthropic prediction for a large multi-jump landscape,” *JCAP* **0810** (2008) 009, [arXiv:0805.3549 \[hep-th\]](#).
- [45] R. Bousso and R. Harnik (*to appear*) .
- [46] M. Tegmark, A. Aguirre, M. Rees, and F. Wilczek, “Dimensionless constants, cosmology and other dark matters,” *Phys. Rev.* **D73** (2006) 023505, [arXiv:astro-ph/0511774](#).
- [47] W. H. Press and P. Schechter, “Formation of galaxies and clusters of galaxies by selfsimilar gravitational condensation,” *Astrophys. J.* **187** (1974) 425–438.
- [48] C. G. Lacey and S. Cole, “Merger rates in hierarchical models of galaxy formation,” *Mon. Not. Roy. Astron. Soc.* **262** (1993) 627–649.
- [49] C. D. Andriessse, “Radiating cosmic dust,” *Vistas in Astronomy* **21** (1977) 107.
- [50] **WMAP** Collaboration, E. Komatsu *et al.*, “Five-Year Wilkinson Microwave Anisotropy Probe (WMAP) Observations: Cosmological Interpretation,” [arxiv:0803.0547 \[astro-ph\]](#).
- [51] M. Tegmark and M. J. Rees, “Why is the CMB fluctuation level  $10^{-5}$ ?,” *Astrophys. J.* **499** (1998) 526–532, [astro-ph/9709058](#).